The boundary of nighttime ozone chemical equilibrium as an indicator of local chemistry disturbances in the polar mesopause region

Mikhail Yu. Kulikov[1], Mikhail V. Belikovich[1], Aleksey G. Chubarov[1], Svetlana O. Dementyeva[1], and Alexander M. Feigin[1]

[1]A. V. Gaponov-Grekhov Institute of Applied Physics of the Russian Academy of Sciences, 46 Ulyanov Str., 603950 Nizhny Novgorod, Russia

Correspondence to: Mikhail Yu. Kulikov (mikhail_kulikov@mail.ru)

Abstract. The nighttime ozone chemical equilibrium (NOCE) is a key assumption widely employed ~~for~~in various applications ~~in~~within the mesopause region, such as retrieving ~~hard~~difficult-to-measure characteristics from ~~observations.~~observational data. Previously, the ~~criterion for determining the~~ NOCE boundary criterion was used to analyze its long-term evolution ~~from~~based on SABER/TIMED data, primarily at low and ~~middle~~ mid-latitudes. This ~~work focuses on~~study extends this focus to polar latitudes. We demonstrate that the NOCE criterion clearly ~~indicates~~delineates the main features of the transition zone ~~separating deep~~ that vertically separates regions of strong and weak ~~O and H~~ diurnal photochemical oscillations of O and H. During the polar night, this transition zone degenerates into a sharp step in ~~their~~the vertical profiles of these species, and the criterion accurately identifies the altitude of this step. ~~Next~~Furthermore, we analyze the evolution of the NOCE boundary using SABER/TIMED ~~data~~observations in conjunction with MERRA-2 reanalysis data for the winter–spring ~~period of~~periods from 2002~~–~~ to 2025. We ~~demonstrate~~show that ~~its~~the most pronounced variability ~~is observed~~of the NOCE boundary occurs at northern polar latitudes during and after strong ~~SSWs with an elevated~~ Sudden Stratospheric Warmings accompanied by stratopause elevation events. Prior to or ~~immediately~~ during the onset of such warmings, the daily mean altitude of the boundary can rise to ~~87~~86 km. ~~Immediately after~~Following these events, it rapidly descends to 72–74 km ~~and~~, where it can remain ~~at this altitude~~ for an extended period. Model studies of the 2009 winter ~~of 2009~~ show that the NOCE boundary closely ~~follows~~tracks the variability of the ~~medians of the~~median vertical distributions of O ~~and~~, as well as the volume emission rates of OH~~*~~,(v=1-9), O~~*~~,(^{1}S), and O_2~~*. Thus, we can assume that the NOCE boundary can be used to monitor significant disturbances in both the O_x HO_x components and the airglows generated by physicochemical processes involving them.~~($b^1\Sigma_g^+$).

1 Introduction

Ozone is a unique atmospheric trace gas that plays different roles depending on altitude. In particular, stratospheric ozone protects life on our planet by absorbing ultraviolet solar radiation in the wavelength range of 200–315 nm. Moreover, by absorbing radiation in the Herzberg continuum, ozone at these altitudes is the only atmospheric minor gas whose vertical distribution determines the

photodissociation rate of the major gas, molecular oxygen. In turn, tropospheric ozone acts as the fourth (in terms of importance) greenhouse gas after H_2O, CO_2 and CH_4. Furthermore, in the boundary layer, ozone is one of the five major pollutants (according to the World Health Organization) that negatively affect the biosphere and human health due to its high toxicity.

In the mesosphere–lower thermosphere (MLT), ozone is involved in reactions between the O_x and HO_x families ($O+O_3$ and $H+OH+HO_2$), which produce many layered phenomena. Below ~80–87 km, there are ~~"deep"~~strong diurnal photochemical oscillations, where the difference between daytime and nighttime values of these components can reach several orders of magnitude due to the diurnal modulation of the photodissociation rates of O_2, H_2O, and O_3. Above ~80–87 km, photochemical oscillations are relatively weak compared to the more pronounced impact of vertical and horizontal transport. As a result, there is a narrow (1–3 km thick) transition region where the regime of photochemical oscillations changes rapidly with height. Above this transition region, O and H concentrations accumulate and reach absolute maxima, forming the corresponding layers, including a layer of stored chemical energy. This leads to the appearance of a secondary ozone maximum and airglow layers of excited OH, O_2 and O observed in the visible and infrared ranges. In particular, the reaction of ozone with atomic hydrogen is the main source of OH airglow, whose intensity spectrum can be used, for example, to derive information about the mesopause temperature. Thus, mesopause photochemistry enables several remote sensing techniques that are widely used for ground-based and satellite monitoring of climate change and wave activity at these altitudes. The chemical heating from exothermic reactions between O_x-HO_x species is one of the major sources of the mesopause energy balance. In particular, this heating can exceed that from turbulent energy dissipation (e.g., Grygalashvyly et al., 2024). Moreover, mesopause photochemistry influences the radiative cooling of this region in the CO_2 15-μm band, is involved in plasma-chemical reactions, and contributes to the formation of ionospheric layers. Note that variations in the O_x-HO_x transition zone height reflect corresponding changes in the O and H layers, and through them, in airglows and other mesopause features. Thus, this characteristic can be considered a sensitive indicator of mesopause processes.

Note also, the mentioned transition of O_x-HO_x behavior with height may occur via the nonlinear response to the diurnal modulation of photodissociation rates, resulting in the appearance of subharmonic (with periods of 2, 3, 4, and more days) or chaotic oscillations of O, O_3, H, OH, and HO_2 (e.g., Sonnemann and Fichtelmann, 1997; Feigin et al., 1998). This unique phenomenon was predicted many years ago (Sonnemann and Fichtelmann, 1987) and further investigated theoretically by taking into account different transport processes (Sonnemann and Feigin, 1999; Sonnemann et al., 1999; Kulikov and Feigin, 2005; Kulikov, 2007; Kulikov et al., 2020), including within the framework of the 3D chemical-transport models (Sonnemann and Grygalashvyly, 2005; Kulikov et al., 2021). The vertical eddy diffusion was revealed as the most important process (Sonnemann and Feigin, 1999; Sonnemann et al., 1999), so that 2-day oscillations can only survive at real diffusion coefficients. At the same time, the eddy diffusion in the zonal

direction leads to the appearance of the so-called reaction-diffusion waves in the form of propagating phase fronts of 2-day oscillations (Kulikov and Feigin, 2005; Kulikov et al., 2012; Kulikov et al., 2020). Recently, the first evidence of 2-day photochemical oscillations in the actual mesopause was revealed through the satellite data processing (Kulikov et al., 2021).

At the MLT altitudes, the physicochemical assumptions involving ozone are useful tool for monitoring poorly measured O_x-HO_x components. In many papers, the rocket and satellite measurements of the ozone and the volume emission rates of OH(v), O(^{1}S), and $O_2(a^1\Delta_g)$ were applied to retrieve O and H distributions (e.g., Good, 1976; Pendleton et al., 1983; McDade ~~et al., 1985; McDade~~ and Llewellyn, 1988; ~~Evans et al., 1988;~~ Thomas, 1990~~; Llewellyn et al., 1993~~; Llewellyn and McDade, 1996; Mlynczak et al., 2007, 2013a, 2013b, 2014, 2018; Smith et al., 2010; Xu et al., 2012; Siskind et al., ~~2008,~~ 2015). The retrieval approach employs a model of the corresponding airglow and an algebraic equation derived from the assumption of ozone photochemical/chemical equilibrium and relating local O and H values with measurement data. The ternary photochemical equilibrium condition of OH, HO_2, and O_3 produces a useful system of algebraic equations, which was used to retrieve daytime distributions O, H, HO_2, and H_2O from simultaneous O_3 and OH data measured during the satellite CRISTA – MAHRSI campaign (Kulikov et al. 2006, 2009) and to evaluate the quality of simultaneous observations OH, HO_2, and O_3 by MLS/Aura (Kulikov et al. 2018a; Belikovich et al., 2019). Note also that the nighttime ozone chemical equilibrium was used (i) to study hydroxyl emission in the MLT region using simulated and measured data, in particular, OH* mechanisms, morphology and variability caused, for example, by atmospheric tides and gravity wave activity (e.g., Marsh et al., 2006; Nikoukar et al., 2007; Xu et al., ~~2010,~~ 2012; Kowalewski et al., 2014; Sonnemann et al., 2015); (ii) to analyze the MLT response to sudden stratospheric warmings (SSWs) (e.g., Smith et al., 2009); (iii) to derive exothermic heating rates in the MLT (e.g., Mlynczak et al., 2013b); (iv) to analytically simulate the mesospheric OH* layer response to gravity waves (e.g., Swenson and Gardner, 1998); and (v) to derive the analytical dependence of excited hydroxyl layer number density and peak altitude on atomic oxygen and temperature (e.g., Grygalashvyly et al., 2014; Grygalashvyly, 2015).

The daytime O_3 balance at MLT altitudes is primarily determined by reactions $O+O_2+M \rightarrow O_3+M$, $O_3 + h\nu \rightarrow O_2+O$, O(^{1}D), and $H+O_3 \rightarrow O_2+OH$ (Kulikov et al., 2017, 2022a). Kulikov et al. (2017) examined O_3 daytime equilibrium within the framework of a 3D chemical-transport model and found it to provide a good approximation everywhere in the MLT region due to the high ozone photodissociation rate. In contrast, nighttime ozone chemical equilibrium (NOCE) is valid above a lower boundary, whose altitude depends on latitude and month. In particular, according to the 3D chemical-transport model, the monthly mean NOCE boundary varies within the range of 81–87 km (Kulikov et al., 2018b). Below this boundary, the local ratio between true O_3 and its equilibrium value may vary widely and reaching several orders of magnitude (e.g., Fig. 5 in Kulikov et al. (2018b)). This means that the error in retrieved data due to the use

of the O_3 equilibrium approximation is uncontrollable and may significantly exceed all other errors in the retrieval procedure arising from, for example, uncertainties in measurement data and rate constants. In order to limit the equilibrium approximation error, Kulikov et al. (2018b) developed a robust analytical criterion that allows localizing the boundary of the NOCE using measured or retrieved data. Kulikov et al. (2019) applied this criterion to determine the NOCE boundary using data from the SABER (Sounding of the Atmosphere using Broadband Emission Radiometry) instrument onboard the TIMED (Thermosphere Ionosphere Mesosphere Energetics and Dynamics) satellite. The space-time distribution of the derived NOCE boundary showed good agreement with model results. Moreover, the application of the NOCE condition below this boundary could lead to a significant (up to 5–8 times) systematic underestimation of the 2-month mean O distribution below 86 km. Recently, Kulikov et al. (2023a) analyzed the long-term evolution of the monthly mean NOCE boundary derived from SABER/TIMED data in 2002–2021. It was revealed that, first, this characteristic at 55°S–55°N contains a clear signal of the 11-year solar cycle and can be considered a sensitive indicator of solar activity. Second, the NOCE criterion at low and middle latitudes reproduces well the altitude and captures the main variations of the transition zone ~~separating deep~~that vertically separates regions of strong and weak diurnal oscillations of O and H. In particular, the transition zone at middle latitudes demonstrates a pronounced annual cycle with minimum altitude in winter and maximum altitude in summer. This is a nontrivial effect as summer nighttime H values are substantially higher than those in winter (e.g., Kulikov et al., 2024), which results in shorter ozone lifetimes in summer than in winter. Thus, one would expect an opposite seasonal dependence of the transition zone altitude. Nevertheless, the same results were obtained in model studies by Belikovich et al. (2018) and Kulikov et al. (2018b). In the work by Kulikov et al. (2023a), the discussed effect was explained by the specific nonlinear properties of nighttime mesopause chemistry, which depend strongly on the daytime O/H ratio preceding the night. By design, the NOCE criterion takes into account these properties, ensuring good agreement with the transition zone position. Thus, this criterion is not only a useful technical tool for retrieving unmeasured data from satellite observations, but also a sensitive indicator of O and H layers. As mentioned, many phenomena in the MLT (e.g., airglows) are caused by O and H layers. Thus, one can expect that variations in the main features of these phenomena (e.g., half-width, peak volume emission rates, etc.) are connected with the NOCE boundary position and can be explained/predicted by the NOCE criterion. Finally, Kulikov et al. (2023a) noted abrupt changes in the NOCE boundary at north polar altitudes in winters with powerful SSWs accompanied by elevated (up to ~80–85 km) stratopause events, but a detailed analysis of these variations was outside the scope of that study.

This article focuses on the local evolution of the NOCE boundary at polar latitudes, primarily during ~~winter.~~ Northern Hemisphere winters characterized by major SSWs. It is well established that SSWs are driven by the upward propagation and amplification of planetary waves from the lower atmosphere and

their subsequent interaction with the stratospheric zonal flow. A major SSW is commonly identified when the winter polar 10-hPa zonal-mean winds poleward of 60°N reverse from westerly to easterly, accompanied by a reversal of the 10-hPa zonal-mean temperature gradient poleward of 60°N (e.g., Butler et al., 2015). In contrast, during a minor SSW, the temperature gradient reverses without a reversal of the background zonal circulation. Consequently, winter processes at mesopause altitudes must be considered within the context of the concurrent dynamics of the upper stratosphere and, in some cases, the lower mesosphere. In the Southern Hemisphere, SSWs are much rarer and weaker than their Northern Hemisphere counterparts (e.g., Vincent et al., 2022). However, a major SSW occurred in September 2002, profoundly affecting the Antarctic ozone hole that year. More recently, a minor SSW in September 2019 exhibited the largest temperature variations ever recorded in the Southern Hemisphere winter polar stratosphere (Roy et al., 2022). Furthermore, the winter of 2024 was characterized by two successive minor SSWs in mid-July and early August (Zi et al., 2025). For broader context, Vincent et al. (2022) identified all minor SSWs in the Southern Hemisphere between 1994 and 2019 using MERRA-2 reanalysis data.

The first goal is to study using model data the connection between the NOCE boundary and the spatiotemporal variability of O_x-HO_x chemistry at these latitudes; the second is to analyze the evolution of the NOCE boundary from the SABER/TIMED dataset during the winter–spring period, especially before, during, and after SSWs in 2002–2025. In the next section, we present the model data used. In Section 3, we briefly describe the criterion for determining the local altitude of the NOCE boundary and explain the methodology of its application to satellite data. In Section 4, we study how the NOCE boundary is related to the features of O and H oscillations calculated by the 3D model. Section 5 presents the main results obtained from SABER/TIMED data in comparison with zonal wind and temperature in the upper stratosphere and lower mesosphere from the MERRA-2 reanalysis. Section 6 is devoted to the discussion, followed by concluding remarks.

2 Used data ~~of 3D models~~

To ~~study~~investigate the ~~connection~~relationship between the NOCE boundary ~~at polar latitudes~~ and the transition zone of O_x-HO_x diurnal oscillations ~~with altitude, we used our calculations~~at polar latitudes, model data with sub-daily temporal resolution are required. The specific year is not critical, as our focus is on these short time scales. To this end, we analyzed a one-year simulation of the NCAR Whole Atmosphere Community Climate Model with thermosphere and ionosphere extension (WACCM-X) (Liu et al., 2018~~). This is a high- top, interactive 3D chemistry-climate model that describes the global evolution of the atmosphere from the surface to $4.1 \cdot 10^{-10}$ hPa at 145 pressure-related altitude levels, with a horizontal resolution of 0.95 degrees in latitude and 1.25 degrees in longitude. The vertical resolution of the model at mesopause altitudes is approximately 1.5 km. The integration step is 5 min. The chemical mechanism includes 74 neutrals and 7 ions, 87 photolysis and photoionization processes, 202 gas-phase~~

~~reactions, and heterogeneous reactions.~~) for the year 2000 as a representative example, using hourly output. We performed the simulation using WACCM-X ~~reproduces many modes of variability and trends in the middle atmosphere, including quasi-biennial oscillations, SSWs, ozone depletion and polar ozone holes, etc.~~

~~To study the impact of the SSW during the winter of 2009 on North Polar chemistry and airglow emissions from excited OH*, O*, and O2* states, we used data from an annual run of the Canadian Middle Atmosphere Model (Scinocca~~(version 2.1) nudged to Modern-Era Retrospective Analysis for Research and Applications, Version 2 (MERRA-2, e.g., Molod et al., ~~2008) provided by the Canadian Centre for Climate Modelling and Analysis. The pressure, temperature, O, H, O_2, and O_3 profiles allowed us to calculate the distributions of OH(v=1-9), O(^{1}S), and O_2($b^1\Sigma_g^+$), according to the airglow models presented by Panka et al. (2021), Gao et al. (2012), and Grygalashvyly et al. (2021), respectively~~2015) data.

To determine the NOCE boundary height, we used version 2.0 of the SABER data product (Level2A) for the simultaneously measured profiles of pressure (p), temperature (T), O_3 (at 9.6 μm), and the total volume emission rate of OH* transitions (9→7 and 8→6) at 2.0 μm at geometrical altitudes. Following Kulikov et al. (2023b), we considered only nighttime data corresponding to solar zenith angles $\chi > 95°$.

As noted above, winter processes at mesopause altitudes must be considered within the context of the concurrent dynamics of the upper stratosphere and, in some cases, the lower mesosphere. Here, we examine the evolution of the NOCE boundary height alongside the zonal-mean wind at 60°N and 10 hPa ($U_{60^{o}N,10hPa}$) and the 10-hPa temperature difference between the polar cap and 60°N ($\Delta T_{90-60^{o}N,10hPa}$). The latter is defined as the difference between the zonal-mean temperature averaged over 80°–90°N and that averaged over 60°–70°N. Both variables were derived from MERRA-2 reanalysis data for the corresponding years. It is worth noting that the use of MERRA-2 data to identify SSWs is a well-established practice.

3 The NOCE criterion and determination of the NOCE boundary from SABER data

~~Here, we repeat the theory behind the NOCE criterion following Kulikov et al. (2023b) to improve the readability of this paper, using the same nomenclature as in the original work.~~

The equilibrium ozone concentration (${O_3}^{eq}$), corresponding to the instantaneous balance between the production and loss terms due to reactions R1 and R2, is given by:

$${O_3}^{eq} = \frac{k_1 \cdot O \cdot O_2 \cdot M}{k_2 \cdot H}, \quad (1)$$

where M is air concentration, and ~~$k_{1,3}$~~$k_{1,2}$ are the corresponding rate constants of the reactions (see Table 1).

Table 1. List of reactions with corresponding reaction rates (for three-body reactions [cm^6 $molecule^{-2}$ s^{-1}], for two-body reactions [cm^3 $molecule^{-1}$ s^{-1}]) taken from Burkholder et al. (2020).

	Reaction	Rate constant
R1	$O+O_2+M \rightarrow O_3+M$	$k_1 = 6.1 \cdot 10^{-34}(298/T)^{2.4}$
R2	$H+O_3 \rightarrow O_2+OH$	$k_2 = 1.4 \cdot 10^{-10} exp(-470/T)$
R3	$O+HO_2 \rightarrow O_2+OH$	$k_3 = 3 \cdot 10^{-11} exp(200/T)$
R4	$H+O_2+ M \rightarrow HO_2+M$	$k_4 = 5.3 \cdot 10^{-32}(298/T)^{1.8}$
R5	$H+HO_2 \rightarrow O_2+H_2$	$k_5 = 6.9 \cdot 10^{-12}$
R6	$H+HO_2 \rightarrow O+H_2O$	$k_6 = 1.6 \cdot 10^{-12}$

As mentioned above, the ~~NOCE~~ criterion for NOCE validity was ~~suggested in~~proposed by Kulikov et al. (2018b). ~~The main idea~~Following a minor correction by Kulikov et al. (2023b), it is ~~that the local values of O_3 and O_3^{eq} are close ($O_3(t) \approx O_3^{eq}(t)$), when τ_{O_3}~~expressed as follows:

$$Crit \equiv \frac{\tau_{O_3}}{\tau_{O_3{}^{eq}}} = 2 \cdot \frac{k_1 \cdot M \cdot O_2}{k_2} \cdot \left(k_4 \cdot M \cdot O_2 \cdot \left(1 - \frac{k_5 + k_6}{k_3}\right) + k_2 \cdot O_3\right) \cdot \frac{1}{k_2 \cdot H \cdot O_3} \ll 1, \quad (2)$$

where k_i are the corresponding reaction rate constants from Table 1, τ_{O_3} is the ozone lifetime and $\tau_{O_3{}^{eq}}$ is the local time scale of $O_3{}^{eq}$~~:~~

~~$\tau_{O_3} = \frac{1}{k_2 \cdot H}$, (2)~~

~~$\tau_{O_3{}^{eq}} \equiv \frac{O_3{}^{eq}}{|dO_3{}^{eq}/dt|} = \frac{O}{H \cdot \left|\frac{d}{dt}\left(\frac{O}{H}\right)\right|}$. (3)~~

~~Kulikov et al. (2018b) determined the expression for $\tau_{O_3{}^{eq}}$ with the use of a simplified photochemical model describing the O_x-HO_x evolution in the mesopause region (Feigin et al., 1998), so the criterion of the NOCE validity is as follows:~~

~~$Cr = \frac{\tau_{O_3}}{\tau_{O_3{}^{eq}}} = 2\frac{k_1 \cdot k_4 \cdot O_2{}^2 \cdot M^2}{k_2}\left(1 - \frac{k_5 + k_6}{k_3}\right) \cdot \frac{1}{k_2 \cdot H \cdot O_3} \ll 1$, (4)~~

~~where k_i are the corresponding reaction constants from Table 1.~~. Calculations ~~with the~~using a global 3D chemistry-transport model of the middle atmosphere showed ~~(Kulikov et al. 2018b)~~ that the criterion ~~$\tau_{O_3}/\tau_{O_3{}^{eq}} \leq Crit =$~~ 0.1 accurately defines ~~well~~ the boundary of the ~~area~~region where $|O_3/O_3{}^{eq} - 1| \leq 0.1$~~.~~

(Kulikov et al~~. (~~., 2018b, 2023b~~) presented~~). Moreover, Kulikov et al. (2023b) developed the theory of chemical equilibrium ~~of~~for a certain trace gas ~~n. Strictly mathematically, the cascade of sufficient conditions for $n_i(t) \cong n_i{}^{eq}(t)$ was derived considering its lifetime, equilibrium concentration, and time dependences of these characteristics. In case of the nighttime ozone, it was proved that $\tau_{O_3}/\tau_{O_3{}^{eq}} \ll 1$ is the main condition for NOCE validity and the criterion $\tau_{O_3}/\tau_{O_3{}^{eq}} \leq 0.1$ limits a possible difference~~

~~between O_3 and O_3^{eq} to not more than ~10%. Moreover, Kulikov et al. (2023b) slightly corrected the expression for the criterion (4):~~and provided a rigorous mathematical proof.

~~$$Cr = 2 \cdot \frac{k_1 \cdot O_2 \cdot M}{k_2} \left(k_4 \cdot M \cdot O_2 \cdot \left(1 - \frac{k_5 + k_6}{k_3}\right) + k_2 \cdot O_3\right) \cdot \frac{1}{k_2 \cdot H \cdot O_3} \leq 0.1. \quad (5)$$~~

~~One more important condition for $O_3 \approx O_3^{eq}$ at~~Since reaction R2 is the ~~time moment t is:~~

~~$$e^{\int_{t_{on}}^{t} \tau_{O_3}^{-1} dt} \gg 1, \quad (6)$$~~

~~where t_{on} is the onset~~source of ~~night. The ozone equilibrium concentration jumps at sunset due to the shutdown of photodissociation. Thus, the condition (6) shows that it takes time for the ozone concentration to reach a new equilibrium. Kulikov et al. (2023b) revealed that, at the solar zenith angle $\chi > 95°$, the condition (6) is fulfilled almost in all cases and the condition (5) becomes the main criterion for NOCE validity. In addition, Kulikov et al. (2023b) demonstrated with the use of a 3-D model that the criterion (5) almost ideally reproduces the NOCE boundary found by direct comparison of O_3 and O_3^{eq} concentrations, see Figure 1 in Kulikov et al. (2023b).~~

~~In the paper, we use version 2.0 of the SABER data product (Level2A) for the simultaneously measured profiles of temperature (T), O_3 (at 9.6 μm), and total volume emission rate (VER) of OH* transitions (9→7 and 8→6) at 2.0 μm within the 0.0001–0.02 mbar pressure interval (altitudes approximately 75–105 km) in 2002–2024. Following Kulikov et al. (2023b), we take into account only nighttime data corresponding to the solar zenith angle $\chi > 95°$.~~

~~Kulikov et al. (2018a) rewrote~~exited OH, the term ~~$k_3 k_2 \cdot H \cdot O_3$~~ in ~~the expression for the NOCE criterion~~(2) can be rewritten in ~~the form depending on measurable~~terms of characteristics ~~only with the use of~~measured by SABER using the corresponding OH(v) model ~~by Mlynczak et al. (2013a):~~:

$$k_2 \cdot H \cdot O_3 = VER/A(T, M, O), \quad (~~7~~3)$$

~~where~~ where VER is the total volume emission rate of OH* transitions (9→7 and 8→6) at 2.0 μm, $A(T, M, O)$ is the function given in square brackets in Eq. (3) ~~in the paper by~~of Mlynczak et al. (2013a~~) with the parameters corrected by Mlynczak et al. (2018):~~

~~$$A(T,M,O) = \frac{0.47 \cdot 118.35}{215.05 + 2.5 \cdot 10^{-11} \cdot O_2 + 3.36 \cdot 10^{-13} \cdot e^{\frac{220}{T}} \cdot N_2 + 3 \cdot 10^{-10} \cdot O} + \frac{0.34 \cdot 117.21}{178.06 + 4.8 \cdot 10^{-13} \cdot O_2 + 7 \cdot 10^{-13} \cdot N_2 + 1.5 \cdot 10^{-10} \cdot O} +$$~~

~~$$\frac{0.47 \cdot 117.21 \cdot (20.05 + 4.2 \cdot 10^{-12} \cdot O_2 + 4 \cdot 10^{-13} \cdot N_2)}{(215.05 + 2.5 \cdot 10^{-11} \cdot O_2 + 3.36 \cdot 10^{-13} \cdot e^{\frac{220}{T}} \cdot N_2 + 3 \cdot 10^{-10} \cdot O) \cdot (178.06 + 4.8 \cdot 10^{-13} \cdot O_2 + 7 \cdot 10^{-13} \cdot N_2 + 1.5 \cdot 10^{-10} \cdot O)}. \quad (8)$$~~

~~).~~ This function is ~~the result of the combination of the equations of~~ derived by combining the physicochemical ~~OH*~~ balance equations for OH* in the v = 8 and v = 9 states~~, in particular,~~ (see Kulikov et al~~. (~~., 2022b~~),~~ for details~~. It depends on the constants of the processes describing sources and sinks at the~~):

$$A(O, M, T) = \frac{f_9 \cdot E_{97}}{E_9 + B_9 \cdot O_2 + C_9 \cdot O + D_9 \cdot N_2} + \frac{f_8 \cdot E_{86}}{E_8 + B_8 \cdot O_2 + C_8 \cdot O + D_8 \cdot N_2} + \frac{f_9 \cdot E_{86}}{E_9 + B_9 \cdot O_2 + C_9 \cdot O + D_9 \cdot N_2} \cdot \frac{E_{98} + B_{98} \cdot O_2 + C_{98} \cdot O + D_{98} \cdot N_2}{E_8 + B_8 \cdot O_2 + C_8 \cdot O + D_8 \cdot N_2}, \quad (4)$$

where f_v are the nascent distributions for vibrational level v; B_v, C_v, and D_v are the total quenching

coefficients for O_2, O, and N_2, respectively, for corresponding level v; E_v are the total spontaneous emission coefficients for corresponding ~~levels, in particular, the OH(v) removal on collisions with O_2, N_2, and O.~~level v; B_{98}, D_{98}, and E_{98} are the quenching ratios for quenching by O_2, N_2, and spontaneous emission coefficients, respectively, for the transitions from level 9 to level 8. The values of these rate constants are given in Mlynczak et al. (2013a), with a correction in Mlynczak et al. (2018). Below 86-87 km, $A(T,M,O) \cong A(T,M,O=0)$~~$\equiv A(T,M)$~~ due to relativity small O concentrations~~.~~ (Kulikov et al~~.~~ (., 2023a~~) verified this approximation by direct comparison of $A(T,M)$ and $A(T,M,O)$ and found it to be valid near the NOCE boundary with mean difference between $A(T,M)$ and $A(T,M,O)$ ~ 0.1%. Thus, by combining Eqs. (5) and (7),~~). Consequently, the NOCE criterion for SABER data can be recast ~~in the following form~~into a form that depends only on measurable characteristics:

$$VER \geq VER_{min}(T,M) \text{~~=~~}\equiv 20 \cdot \frac{k_1 \cdot O_2 \cdot M}{k_2}\left(k_4 \cdot M \cdot O_2 \cdot \left(1 - \frac{k_5+k_6}{k_3}\right) + k_2 \cdot O_3\right) \cdot A(T,M\text{~~).~~}$$

~~(9~~

~~,$O = 0$),~~ (5)

~~One can see that,~~ where VER_{min} ~~decreases rapidly with height due to the strong (~M^4) air-concentration dependence. So, this inequality is well fulfilled at 105 km, but the relationship at 70-75 km is inverse. The~~ is the total volume emission rate at which the condition $\tau_{O_3}/\tau_{O_3}{}^{eq} = 0.1$ is satisfied. Thus, the local position of the NOCE boundary (~~geometrical~~ altitude ~~level~~ z_{eq}) is determined ~~according to the~~using criterion (~~9~~5), where $VER = VER_{min}(T,M)$. In the zeroth approximation (see Table 1):

$$VER_{min} \approx 20 \cdot \frac{k_1 \cdot k_4 \cdot {O_2}^2 \cdot M^2}{k_2} \cdot A(T,M,O=0) \sim \frac{k_1 \cdot k_4}{k_2} \sim exp(470/T)/T^{4.2}, \quad (6)$$

which ensures a strong anti-correlation between z_{eq} and temperature (Kulikov et al., 2023a): cooling of the mesopause leads to a noticeable rise in z_{eq}, and vice versa. Kulikov et al. (2023b) ~~studied~~investigated the uncertainty ~~of the~~in z_{eq} retrieved ~~NOCE boundary height.~~from SABER data. Following the ~~typical~~standard error analysis presented, for example, in Mlynczak et al. (2013a, 2014), the uncertainty was obtained by calculating the root-sum-square of the individual ~~sensitivity~~sensitivities of the retrieved characteristic to ~~the perturbation of~~ perturbations in O_3, T, reaction rates ~~of reactions~~, and the parameters of the A function. As ~~the~~a result, the uncertainty in the local altitude of the NOCE boundary ~~local height~~ was found to ~~be varied~~vary in the range of 0.1~~–~~–0.3 km.

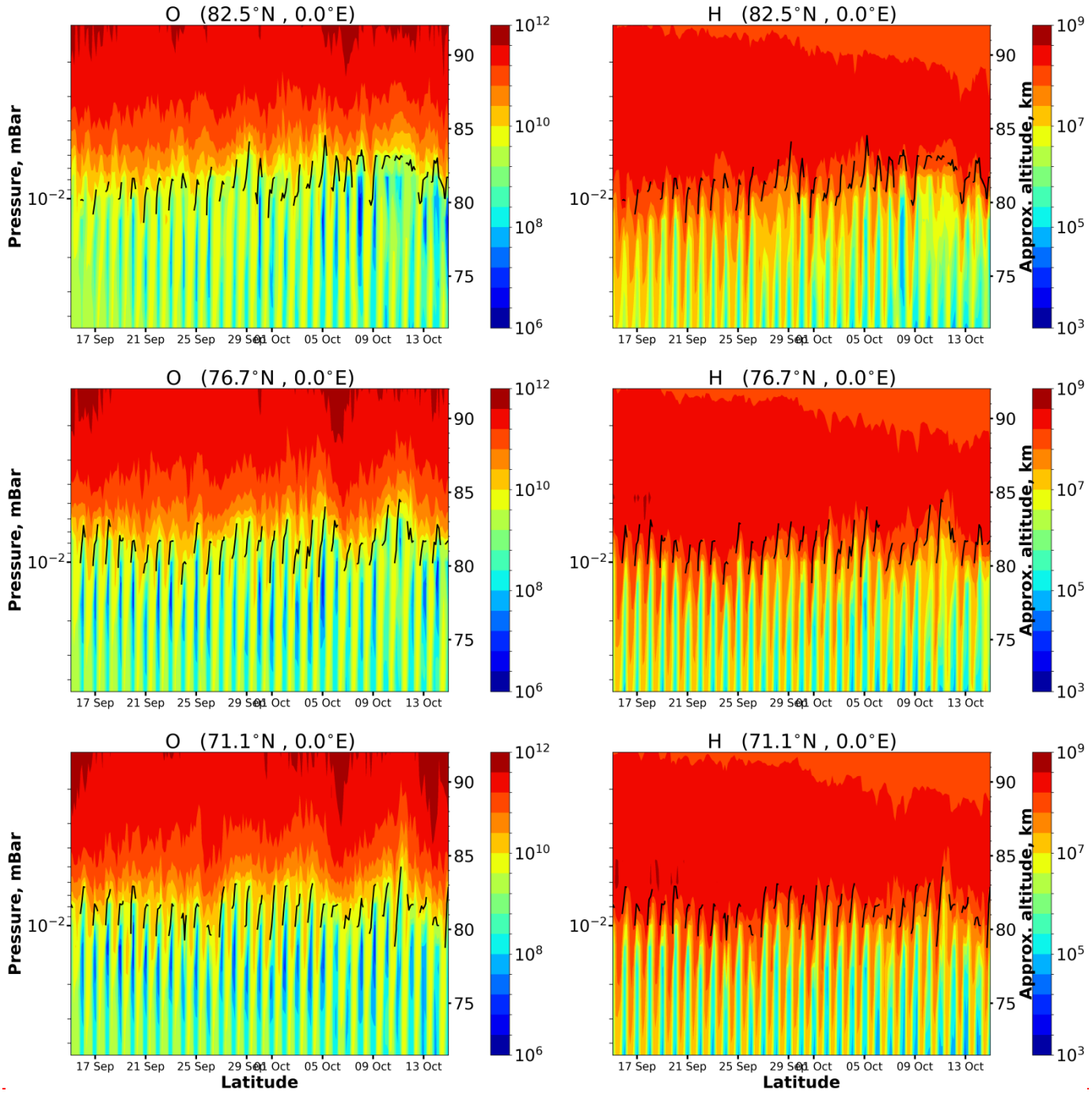
In this paper, we use the function $A(T,M,O)$ with updated rate constants corresponding to the OH(v) model of Panka et al. (2021). In particular, the quenching rates of OH(v = 8, 9) by O_2, N_2, and O were adopted from Adler-Golden (1997) and Caridade et al. (2013), respectively. Furthermore, the model accounts for the multiquantum quenching of OH* via the process OH($v \geq 5$) + O(^{3}P) → OH($0 \leq v' \leq v\text{-}5$) + O(^{1}D), as described by Sharma et al. (2015) and Kalogerakis et al. (2016). Applying criterion (5), we processed all simultaneous vertical profiles of p, T, O_3, and VER ~~from~~ at geometric altitudes from the

SABER database for the period 2002 ~~to~~ 2025 ~~and determined~~, determining the position of the NOCE boundary as a function of time, latitude, and longitude. Additionally, the concentration of M was calculated using the ideal gas law, while the spatiotemporal distribution of the O_2 mixing ratio was adopted directly from the SABER database processing. The latitude range from 82.5°S to 82.5°N was divided into 33 bins 5° each, and all local values of z_{eq} falling into a given bin on a specific day of the year were averaged. Then, we calculated daily mean values of ${z_{eq}}^{d}$ (hereafter, the superscript d denotes the daily average).

4 The connection of the NOCE boundary with spatiotemporal variability of O_x-HO_x chemistry

Figures 1–3 demonstrate the day-to-day evolution of O and H as a function of altitude above various northern polar locations over 3.5 months (from mid-September to December ~~2017~~2000), as simulated by WACCM-X. Thus, Figures 1 and 3 correspond to periods around the autumnal equinox and the winter solstice, respectively. From mid-September to mid-October, pronounced diurnal O and H oscillations occur below 79–80 km, where nighttime values drop by several orders of magnitude relative to daytime values. These oscillations are driven by variations in solar radiation and high nighttime loss rates of HO_x and O, which are nonlinearly dependent on air concentration. Above 83–85 km, the behavior of O and H is fundamentally different. First, the diurnal range between minimum and maximum values is significantly reduced. Second, variations on multi-day timescales predominate in the corresponding spectra. The two ~~modes~~regimes (upper and lower) of O and H ~~behavior~~oscillations are connected vertically by a transition zone several kilometers thick, which is characterized by sharp vertical gradients in the ~~mean~~ daily mean concentrations of these species. Note that the black lines in Figures 1–3 indicate the NOCE boundary according to criterion (5). An interesting feature is observed in the dynamics of the $\mathrm{Cr} = 0.1$ contour line, which is typical of most nights in Figure 1. Over the course of a single night, this line traverses the transition zone, moving from its lower part, where the ~~lower mode of~~strong O and H ~~behavior~~oscillations still ~~persists~~persist, to the upper part of the transition zone, where the ~~upper mode is~~weak O and H oscillations are already established. Thus, as at middle and low latitudes (see Kulikov et al., 2023a), the NOCE criterion clearly indicates the local position and thickness of the transition zone. The duration of daylight decreases as the year progresses; this manifests relatively weakly in the upper region, but strongly in the lower region. Specifically, below the transition zone (see Figure 2), the mean daily concentrations of O and H decrease noticeably, and their diurnal oscillations become less pronounced or periodically disappear (i.e., they are obscured by variations on other timescales). This is especially noticeable at 82.5°N. Finally, in December (see Figure 3), the mean daily concentrations of O and H at lower altitudes drop to such low levels that the transition zone effectively "degenerates" into a step in the vertical profiles of these species, and the NOCE criterion marks the altitude of this transition. It should be noted that below 75 km, diurnal oscillations remain noticeable, ~~which is likely due to a combined effect of atmospheric~~

~~dynamics and chemical relaxation~~likely due to residual photodissociation (e.g., of O_3, Figures S1 in the Supplement) under twilight conditions. The same diurnal oscillations of O and H can be found in other runs of the WACCM-X model, e.g., https://doi.org/10.26024/5b58-nc53.



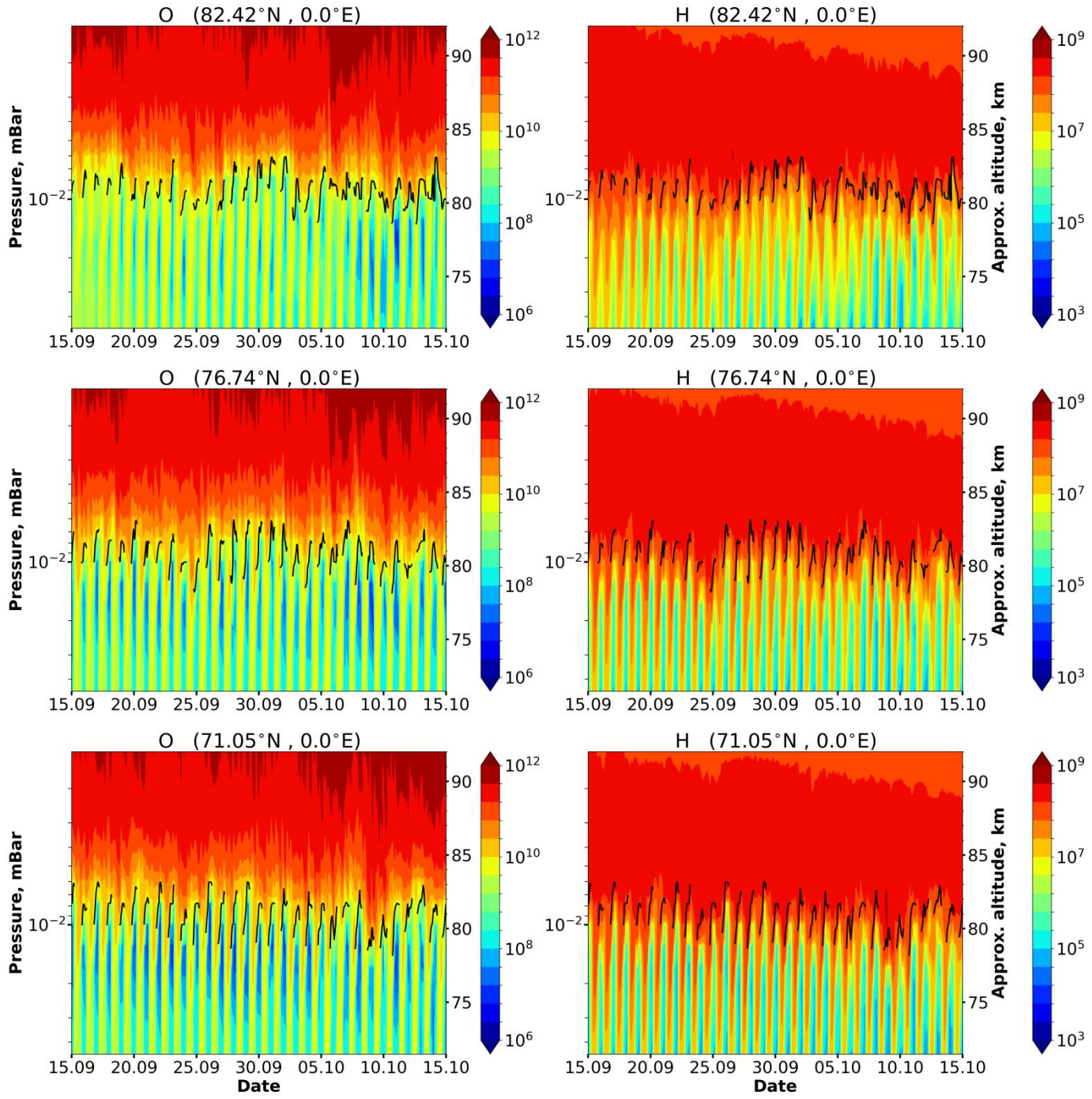
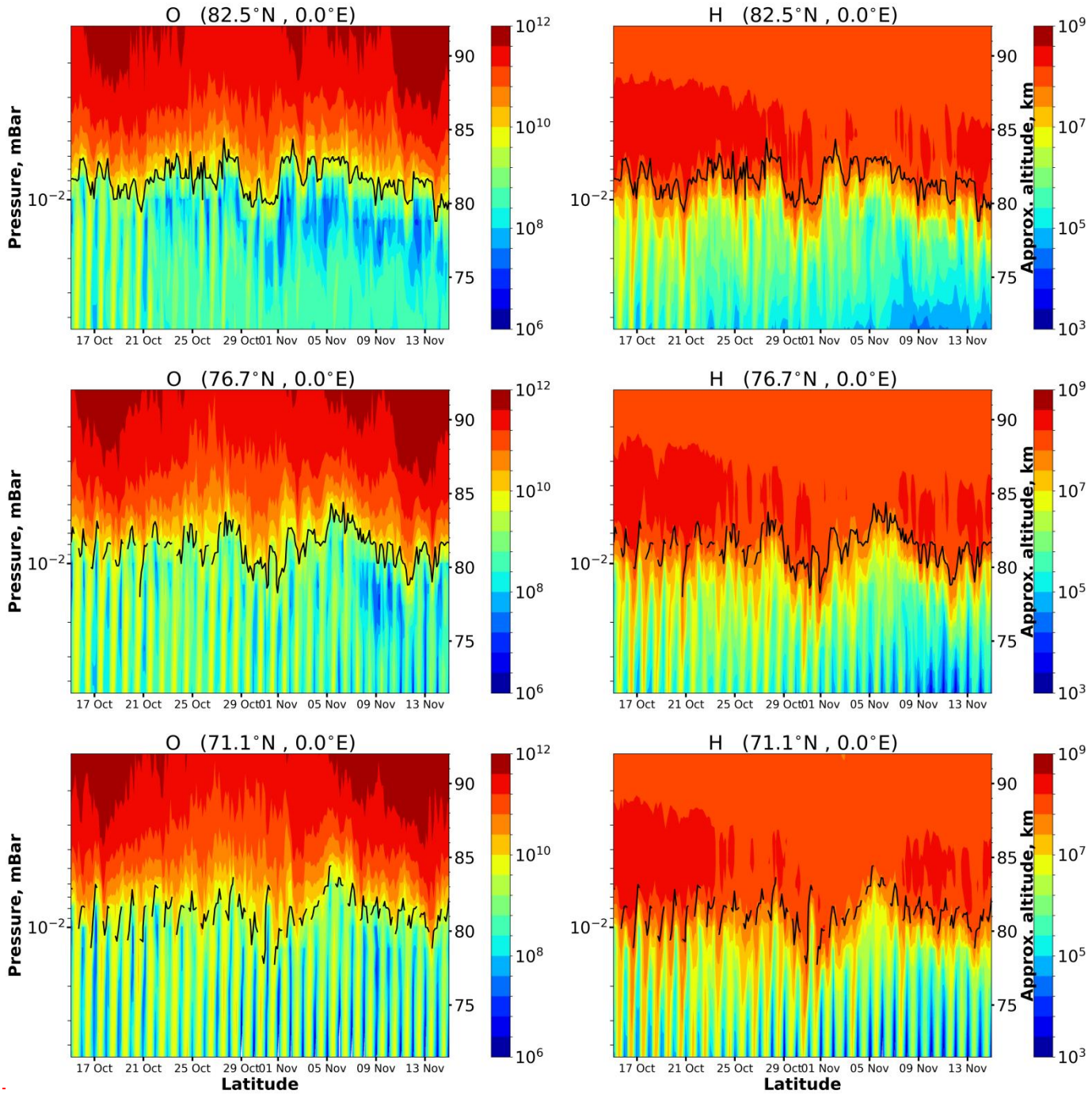


Figure 1. ~~O and H time~~Time-height variations ~~above different~~of O and H (in cm^{-3}) over various polar ~~points~~locations in September~~-~~October ~~2017~~2000, calculated ~~by~~using the 3D chemical transport model ~~WACC~~WACCM-X. Log-pressure altitude is used as the vertical coordinate. Black lines ~~point~~indicate the NOCE boundary altitude ~~in accordance to~~based on criterion (5) (Cr = 0.1).


O (82.5°N , 0.0°E)
H (82.5°N , 0.0°E)
O (76.7°N , 0.0°E)
H (76.7°N , 0.0°E)
O (71.1°N , 0.0°E)
H (71.1°N , 0.0°E)
Pressure, mBar
Approx. altitude, km
Latitude
17 Oct
21 Oct
25 Oct
29 Oct
01 Nov
05 Nov
09 Nov
13 Nov

343

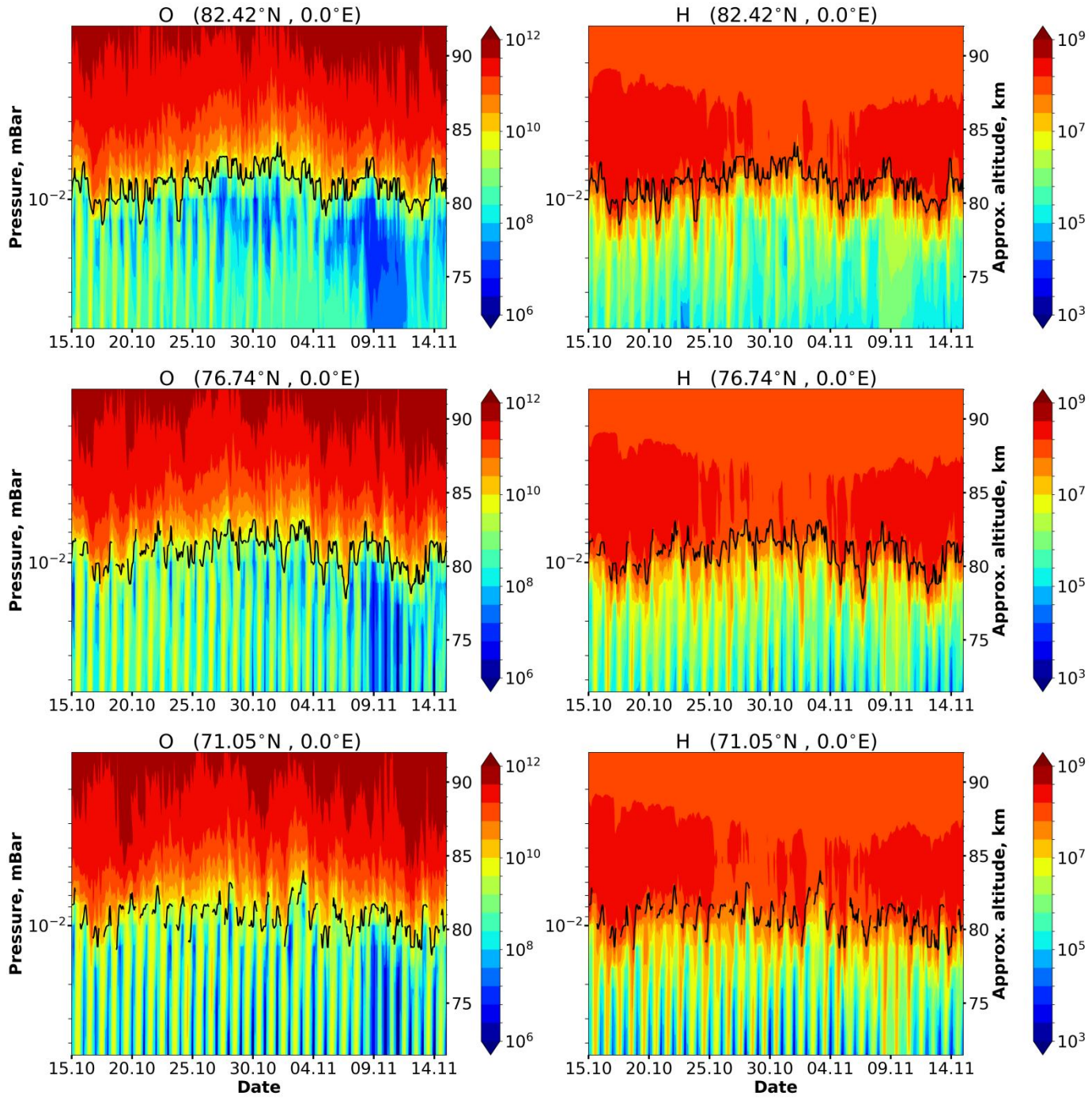
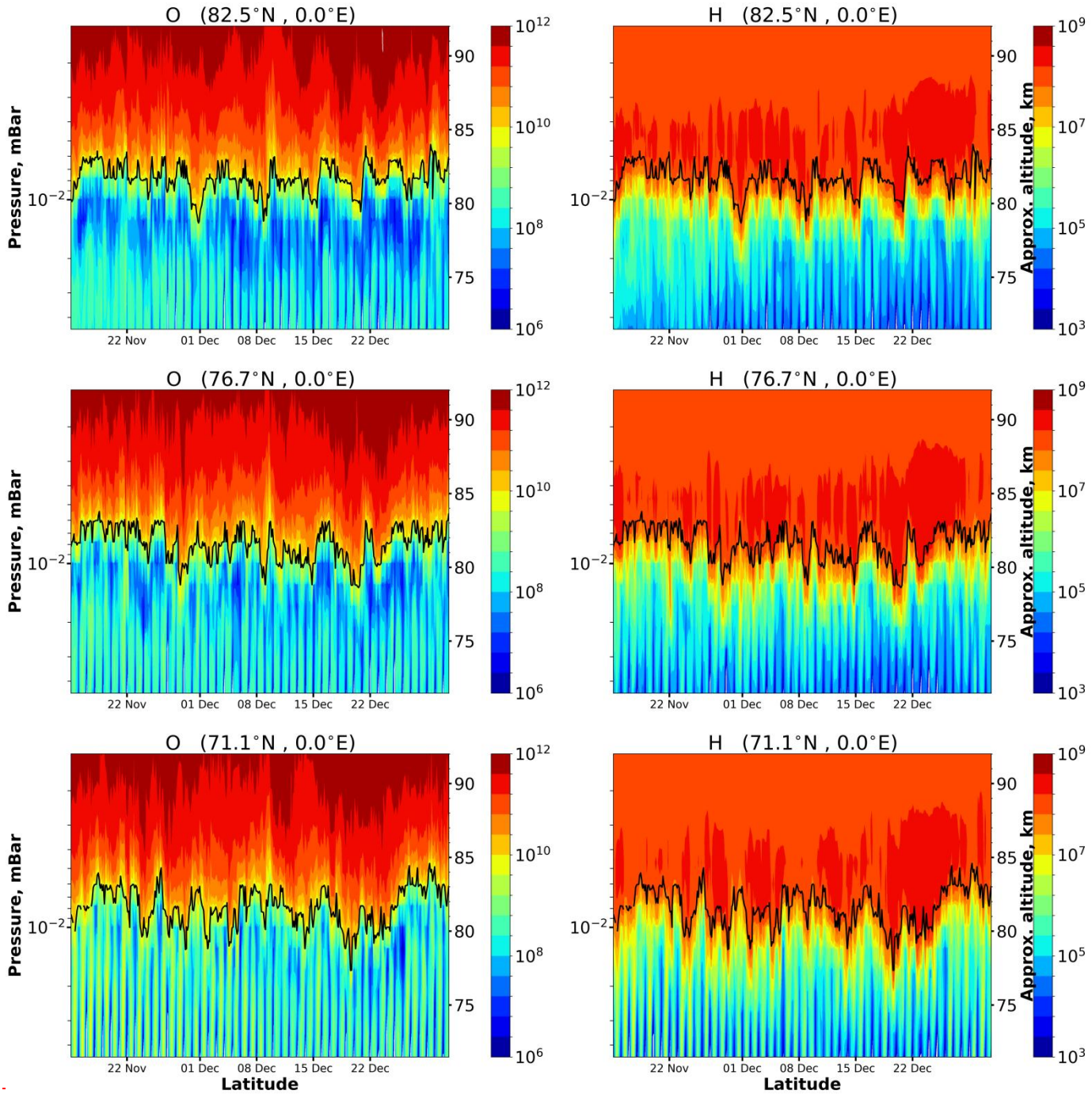


Figure 2. The same as in Fig. 1, but in October – November 2000.


O (82.5°N , 0.0°E)
H (82.5°N , 0.0°E)
O (76.7°N , 0.0°E)
H (76.7°N , 0.0°E)
O (71.1°N , 0.0°E)
H (71.1°N , 0.0°E)
Pressure, mBar
Approx. altitude, km
22 Nov
01 Dec
08 Dec
15 Dec
22 Dec
Latitude

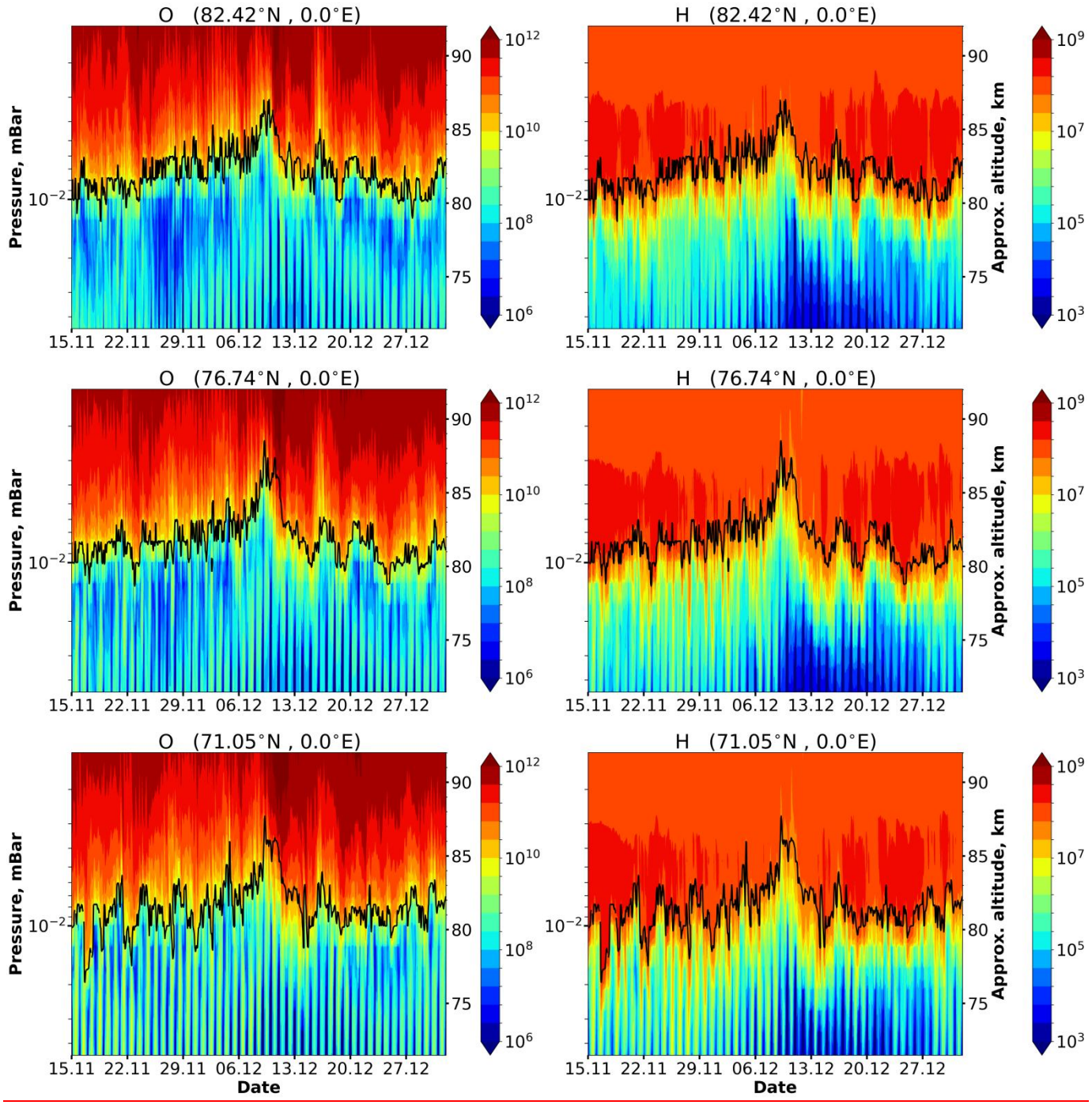
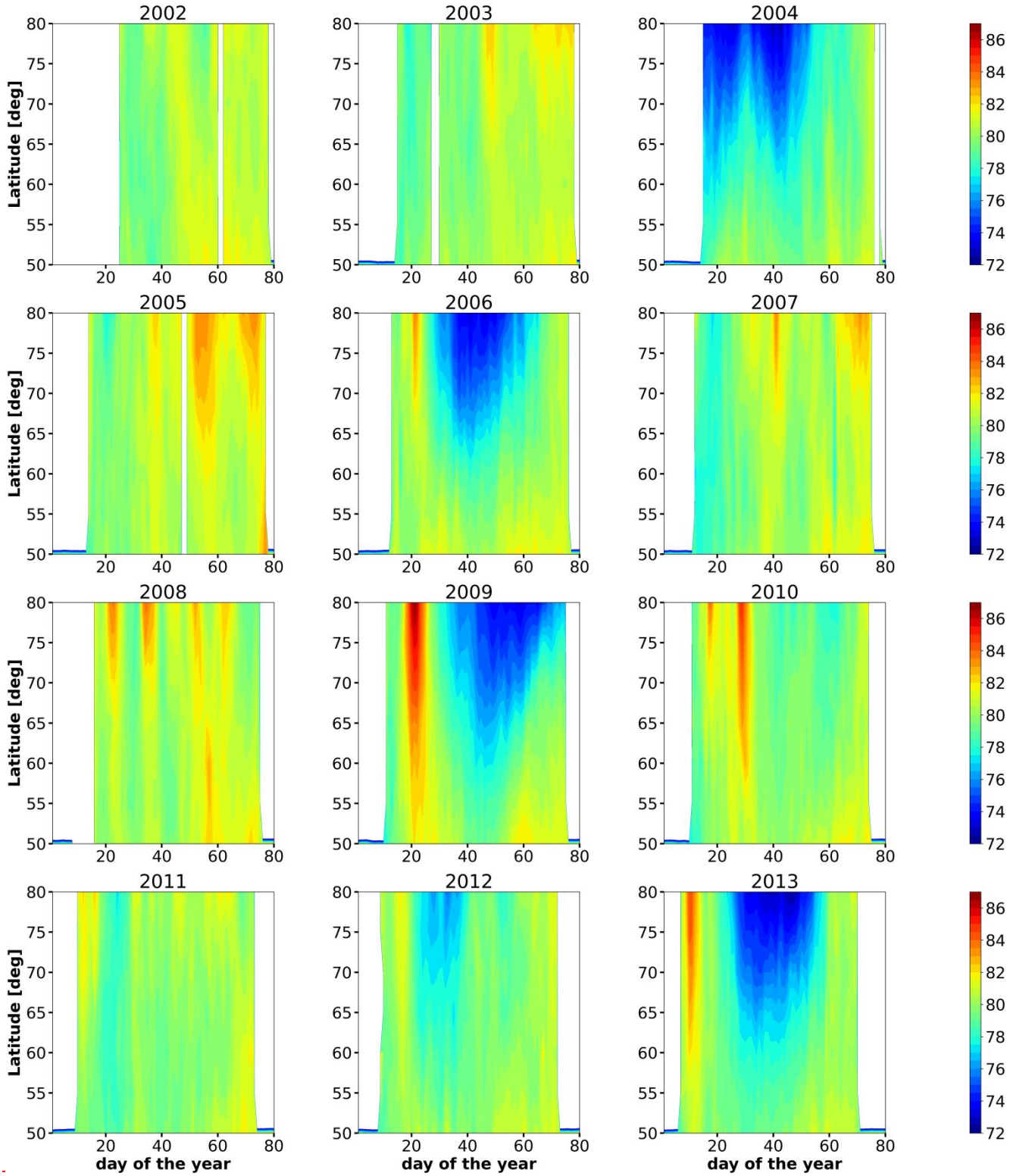


Figure 3. The same as in Fig. 1, but in November ~~–~~ December 2000.

5 NOCE boundary in the polar winters of 2002-2025 from SABER/TIMED data: main results and discussion

Figures 4~~-~~ and 5 present contour maps showing the ~~northern~~ latitude–time evolution of ~~$z_{eq}{}^{d}$ from January to March between 2002 and 2025~~$z_{eq}{}^{d}$ in the Northern Hemisphere during the winter–spring period from 2002 to 2025, derived from SABER data. The strongest disturbances ~~can be seen above 60ºNare observed~~ in ~~early~~ 2004, 2006, 2009, 2010, 2012, 2013, and 2019. These ~~winters~~years are ~~known for~~characterized by remarkable ~~major~~ SSWs followed by elevated stratopause (ES) events. ~~In~~During other

winters, ~~there were no~~ such strong ~~warming events, but~~ warmings did not occur; however, a notable single pulse of $z_{eq}{}^{d}$ ~~may occur~~was observed (see, e.g., 2020), ~~when it rose by several kilometers~~or multi-pulse behavior occurred (e.g., in 2008 and ~~returned to its original level within 7-10 days, as well as quasi-periodical oscillations (see 2008) with a~~2015). The variations in $z_{eq}{}^{d}$ are most pronounced at 80°N and decrease toward the midlatitudes; however, in some years (e.g., 2009), they extended to 50°–60°N. To identify the characteristic ~~period~~features of ~~~10-15 days.~~ $z_{eq}{}^{d}$ during these years and their underlying causes, we examine its time evolution at 80°N alongside the zonal mean wind at 60°N and 10 hPa ($U_{60^{o}N,10hPa}$) and the temperature difference between the pole and 60°N at 10 hPa ($\Delta T_{90-60^{o}N,10hPa}$). As mentioned previously, both variables were calculated using MERRA-2 reanalysis data for the corresponding years. Furthermore, we correlate variations in $z_{eq}{}^{d}$ with the height-time evolution of temperature in the stratosphere and mesosphere at 80°N, using data from SABER observations (Figures S2-S5 in the Supplement) and the JAWARA reanalysis (Yamazaki et al., 2025).


2002
2003
2004
2005
2006
2007
2008
2009
2010
2011
2012
2013
Latitude [deg]
day of the year
80
75
70
65
60
55
50
20
40
60
80
86
84
82
80
78
76
74
72

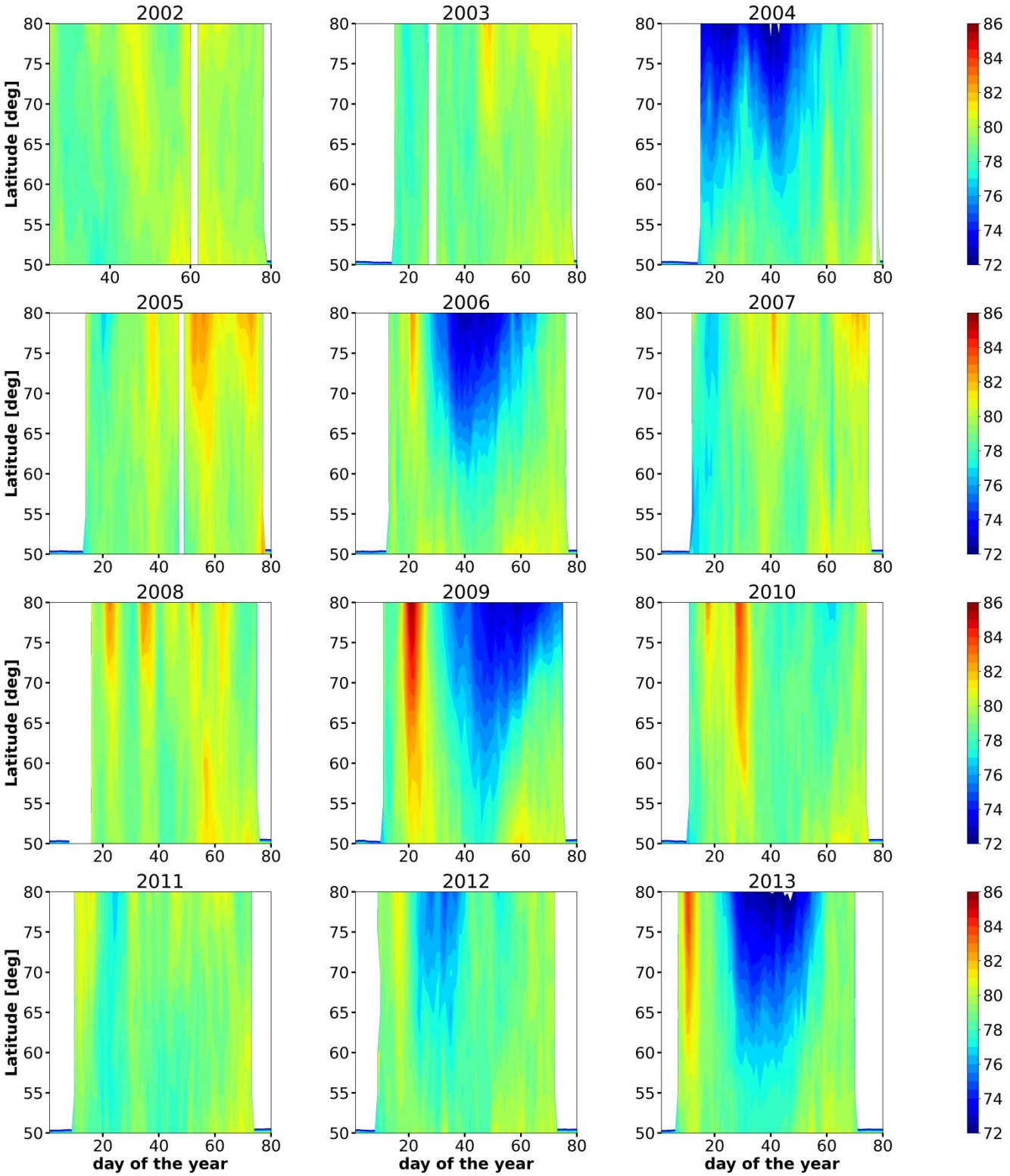
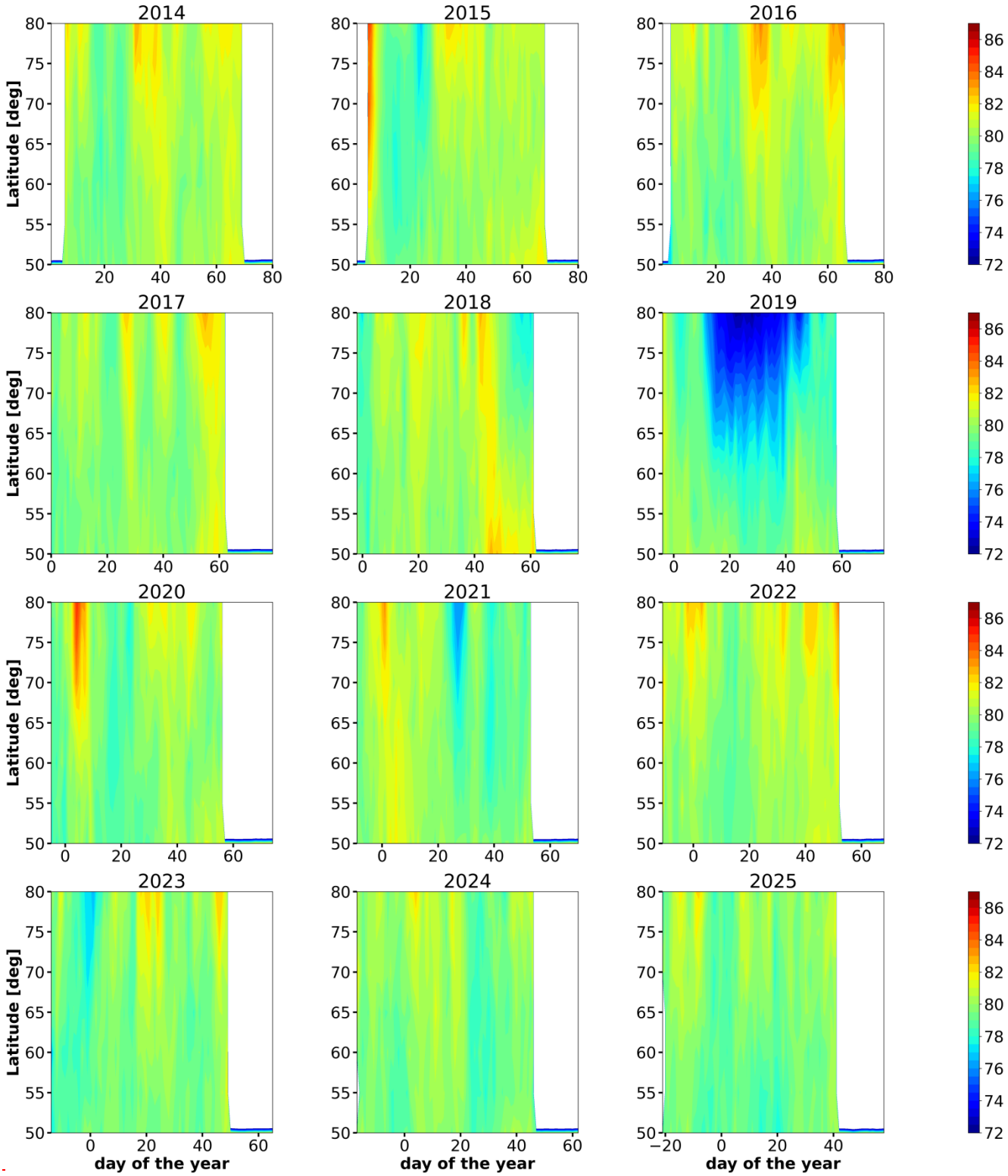


Figure 4. Latitude-time evolution of the daily mean NOCE boundary $z_{eq}{}^{d}$ (geometrical altitude, km) at northern polar latitudes in ~~different years~~2002-2013 obtained from SABER data. White areas indicate missing data due to satellite geometry.


2014
2015
2016
2017
2018
2019
2020
2021
2022
2023
2024
2025
Latitude [deg]
day of the year

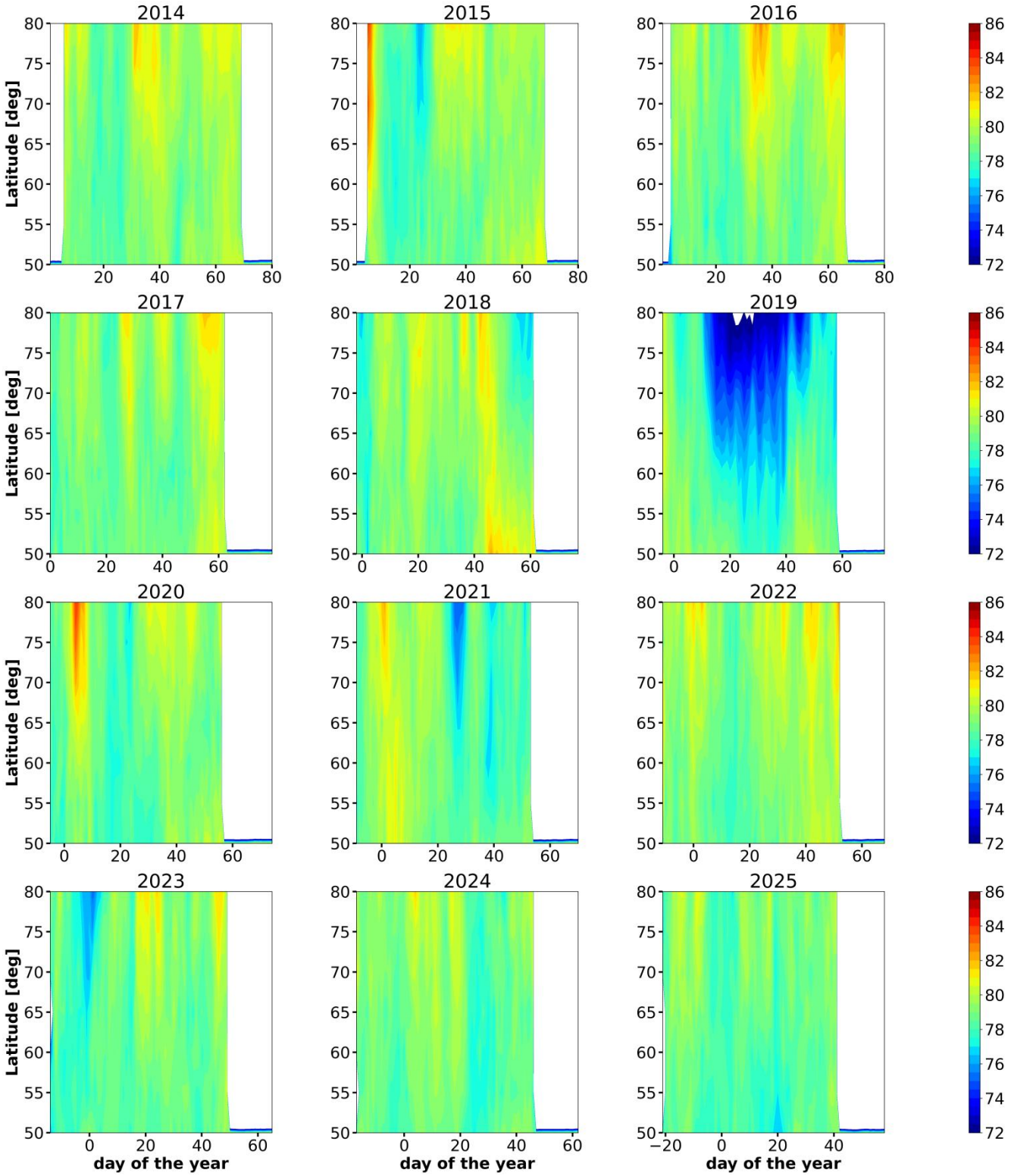
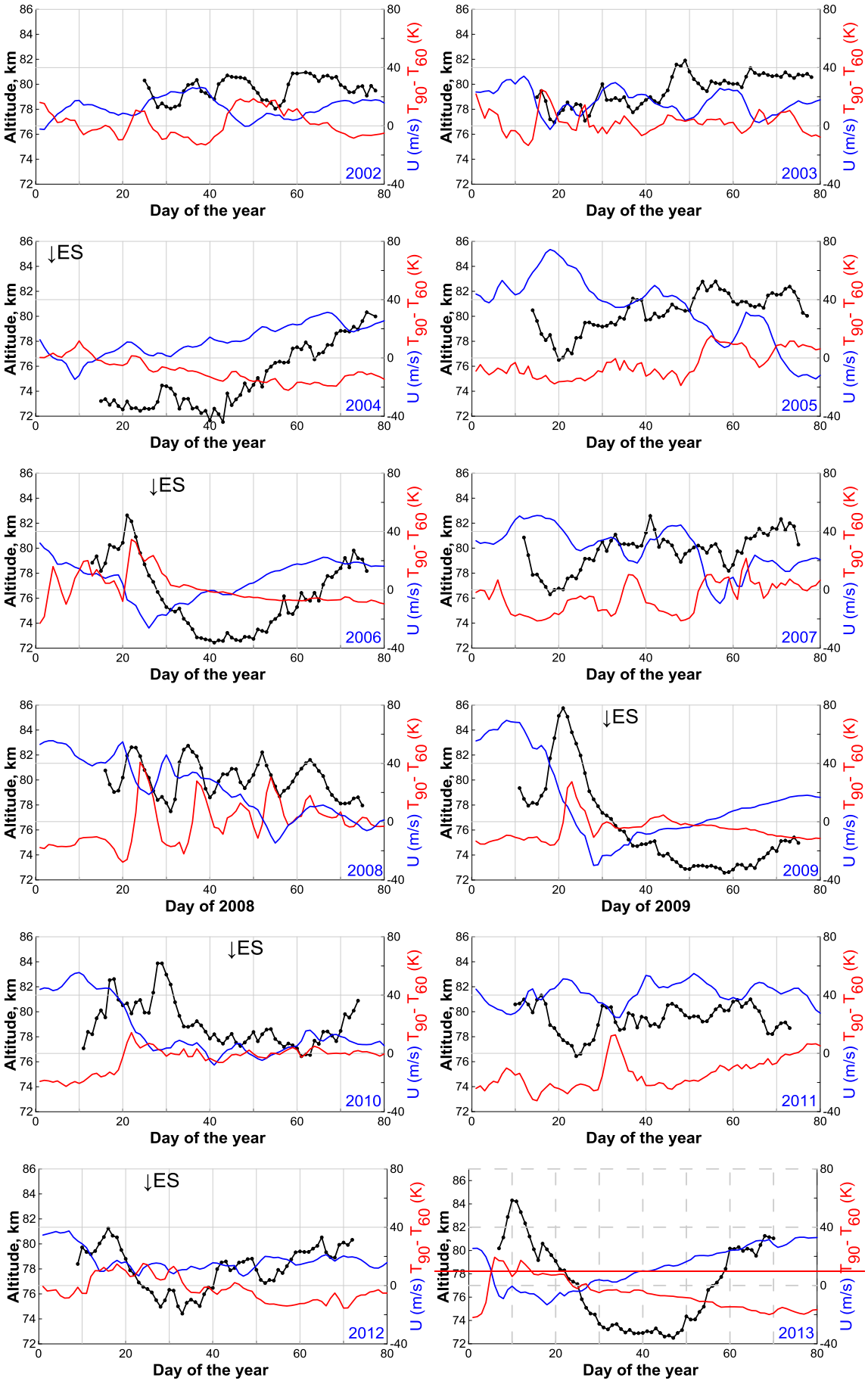


Figure 5. ~~Latitude-time evolution of the daily mean NOCE boundary $z_{dq}{}^{d}$ at northern polar latitudes in different years.~~Same as Figure 4, but for the period 2014–2025.


2002
2003
↓ES
2004
2005
↓ES
2006
2007
↓ES
2008
2009
↓ES
2010
2011
↓ES
2012
2013
Altitude, km
Day of the year
Day of 2008
Day of 2009
U (m/s) T90- T60 (K)

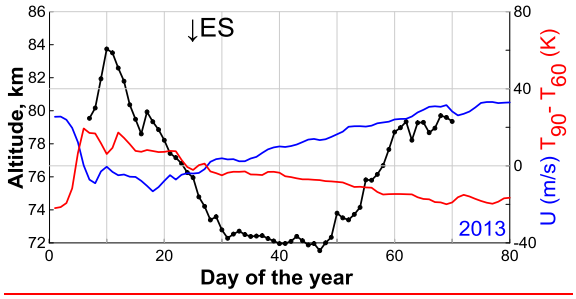
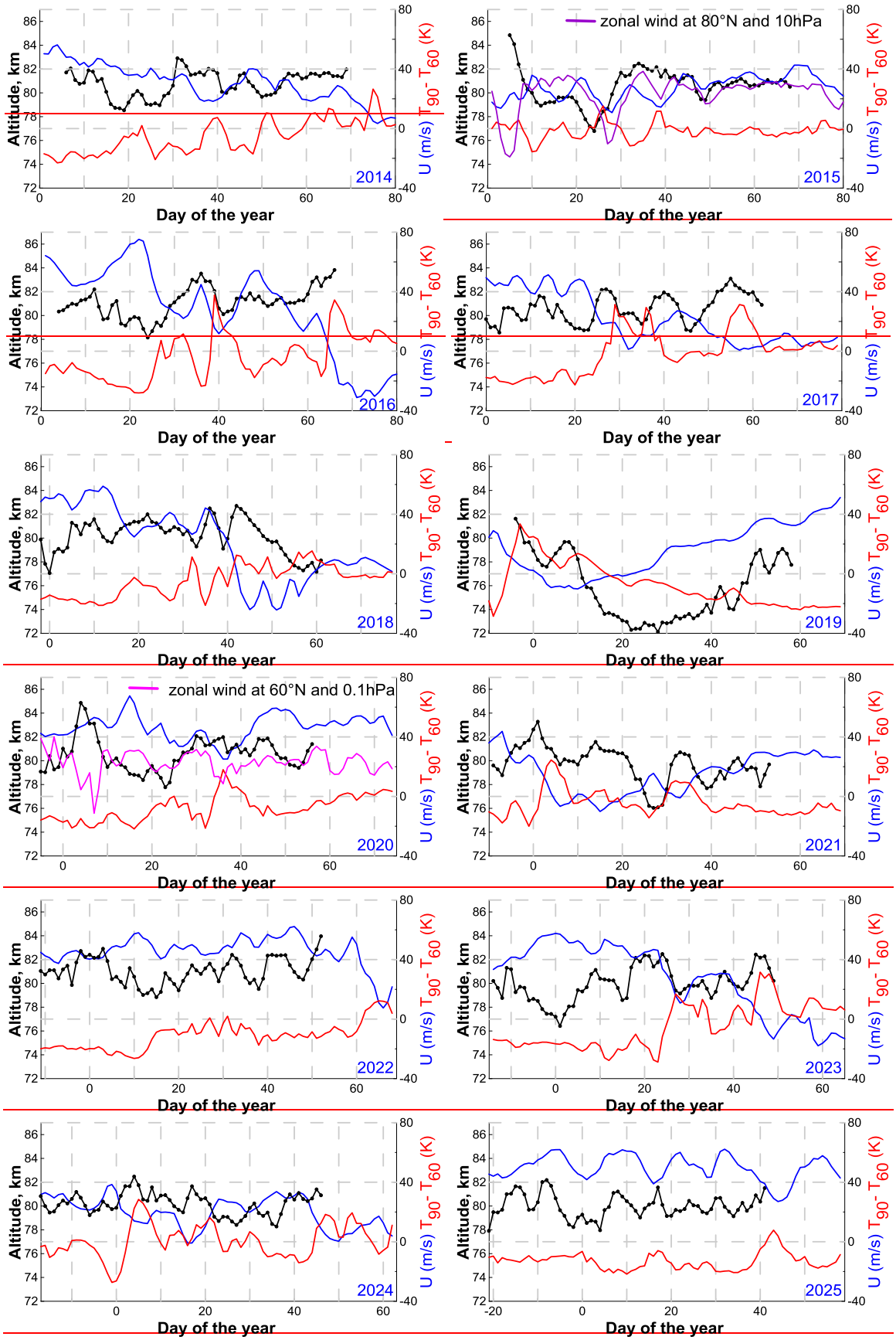


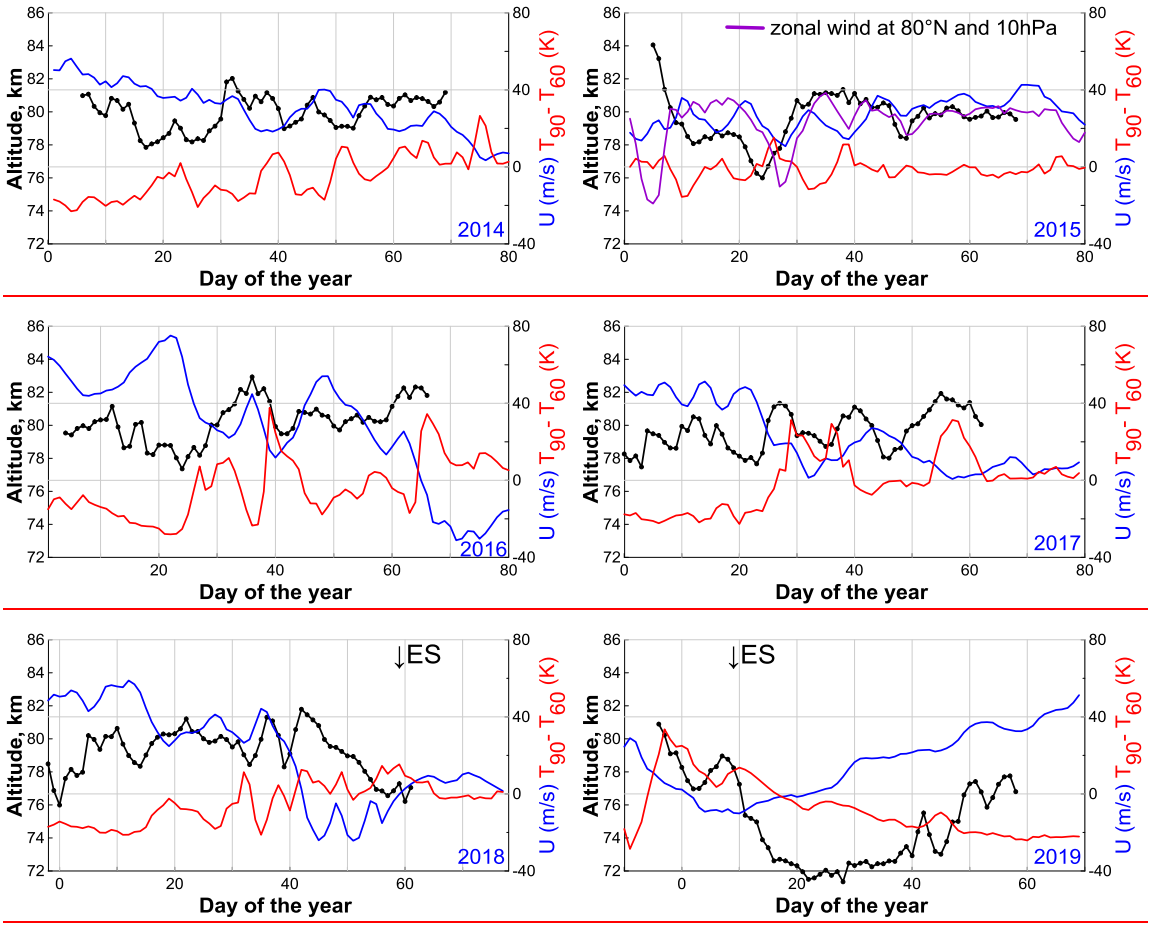
Figure 6. Time evolution of $z_{eq}{}^{d}$ ~~at 80ºN in different years~~ (geometrical altitude) at 80°N during 2002–2013, derived from SABER data (black lines with dots~~). The blue~~, left y-axis). Blue lines ~~show~~represent the zonal mean wind at ~~60ºN~~60°N and ~~10hPa, the~~10 hPa (right y-axis), while red lines ~~show~~indicate the pole-to-60°N temperature difference ~~between the pole and 60ºN at 10hPa.~~



~~Figure 7. Time evolution of z_{aq}^{d} at 80ºN in different years (black lines with dots). The blue lines show the zonal mean wind at 60ºN and 10hPa, the red lines show the temperature difference between the pole and 60ºN at 10hPa.~~

~~It is well known that SSWs~~at 10 hPa (right y-axis); both variables are ~~caused by the amplification of planetary waves traveling from the lower atmosphere and their interaction with the zonal flow at stratospheric altitudes. Therefore, winter processes at mesopause altitudes should be considered in the context of the simultaneous dynamics of the upper stratosphere and, in some cases, the lower mesosphere. Therefore, in Figures 6-7, the evolution of z_{eq}^{d} at 80ºN is shown together with the dynamics of the zonal mean wind at 60ºN and 10hPa ($U_{60ºN,10hPa}$) and the temperature difference ($\Delta T_{90-60ºN,10hPa}$) between the pole and 60ºN at 10hPa, defined as the difference between the average temperatures in the latitudinal ranges of 80-90ºN and 60-70ºN. Both characteristics were calculated using~~ from the MERRA-2 reanalysis ~~data for~~. The "↓ES" symbol marks the onset of the ES event in the corresponding years~~.~~, as identified, for example, by Yamazaki et al. (2025).

~~In the winter of 2001/2002, there were two major SSWs on 29-Dec-01 and 17-Feb-02, respectively. The satellite geometry of SABER measurements above 55°N allowed us to determine z_{eq}^{d} only from the end of January, tracking the last major event. During this SSW, we observe weak variations in z_{eq}^{d} within the range of 78.5-81.5 km without~~



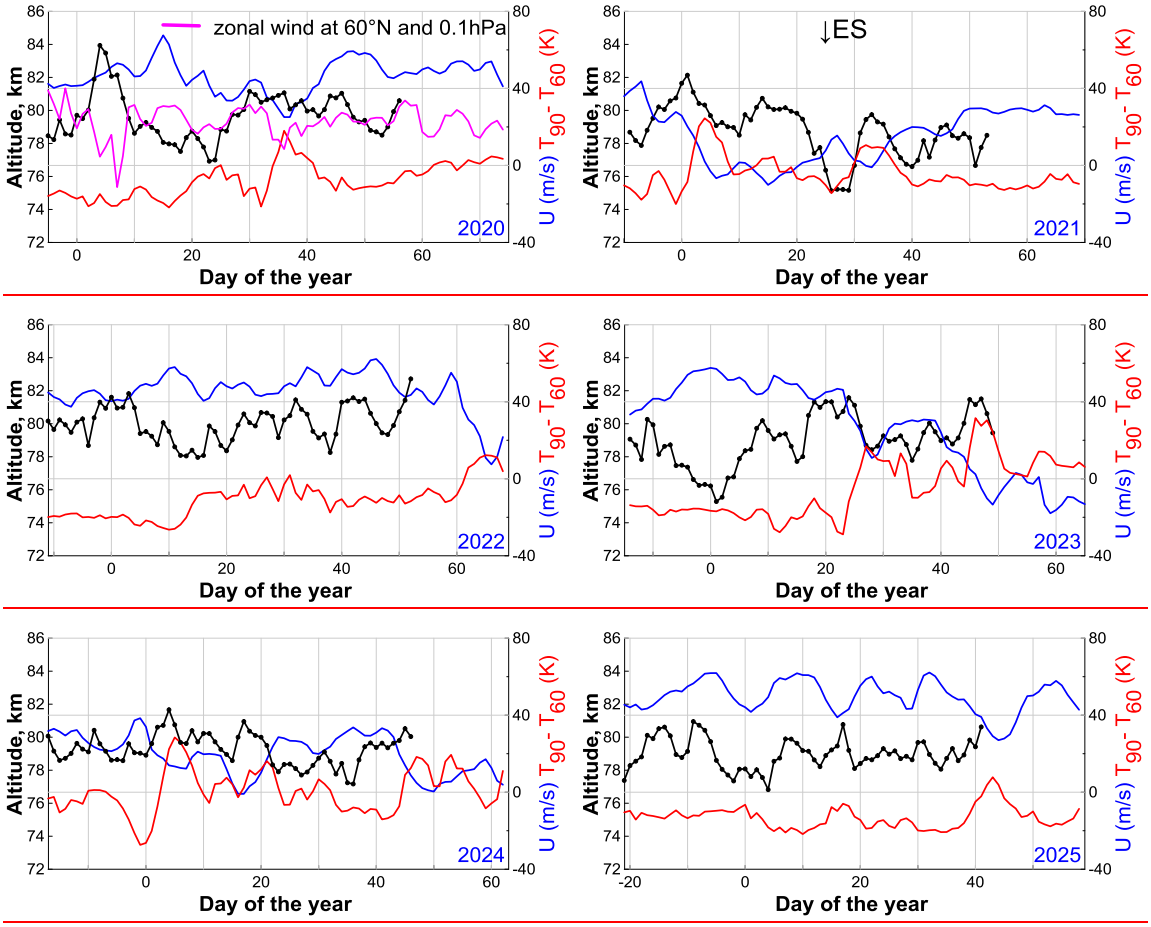


Figure 7. Same as Figure 6, but for the period 2014–2025. Additional data in the 2015 and 2020 panels are derived from the MERRA-2 reanalysis.

As shown in Figures 6 and 7, in years without ES events, ${z_{eq}}^{d}$ typically varied within the 78–82 km range. Furthermore, the influence of major or minor SSWs is not clearly evident. In general, the dynamics of ${z_{eq}}^{d}$ show no distinct regularity, nor do they exhibit a clear correlation with $U_{60ºN,10hPa}$ or $\Delta T_{90-60ºN,10hPa}$.

~~In the 2002/2003 winter, a major SSW occurred on 18 January; however, due to the late start of dataset, it is impossible to see how it manifested at mesopause altitudes. Only a slight oscillation in ${z_{eq}}^{d}$ can be seen in the final stage of this event. Note that in mid-February, there was a strong (nearly to zero) weakening of the zonal wind followed by its recovery, which was accompanied by a~~This is particularly noticeable ~~local increase of ${z_{eq}}^{d}$ against the background of a slow seasonal trend.~~

~~The winter of 2003/2004 was notable in the 40-year record of meteorological analyses (Manney et al., 2005). A powerful major SSW occurred on January 5, after which the phenomenon of an elevated stratopause was first recorded. Evidently, the pronounced low values of ${z_{eq}}^{d}$ at 80°N (down to ~72.5 km, see Figure 6) from January 15 onwards were caused by this event. Starting in mid-February, ${z_{eq}}^{d}$ began to recover, reaching ~80 km at the end of the dataset.~~

~~The winter of 2004/2005 was characterized by a strong~~ in years with a relatively weak polar vortex~~, and no major SSW was detected before the final stratospheric warming on March 11. However, it can be noted that, unlike the cases of 2001/2002 and 2002/2003, the variations in $z_{eq}{}^{d}$ demonstrated better agreement with the upper stratospheric dynamics. A comparison of the $z_{eq}{}^{d}$ evolution with $U_{60°N,10hPa}$ shows a good correlation with a coefficient of approximately -0.8. In particular, the absolute minimum in $z_{eq}{}^{d}$ on 20 January corresponded to a zonal wind increase to 70 m/s, whereas two $z_{eq}{}^{d}$ maxima on days ~55 and ~70 could be caused by a local deep minimum and reversal (<0 m/s) of the zonal wind~~ (e.g., 2002, 2003, 2014, 2021, and 2024). However, three notable exceptions are evident in 2008, 2015, and 2020.

~~In 2005/2006, the central date of the major SSW was January 21, which corresponded to a noticeable rise in $z_{eq}{}^{d}$ from ~79 km to ~83.5 km. The subsequent rapid drop of this characteristic to ~73 km in February and the following rise to 80–81 km in March can be attributed to the appearance and subsequent disappearance of an elevated stratopause. According to Yamazaki et al. (2025), during this SSW, the stratopause jumped from ~30 km to ~80 km around January 25.~~

~~In 2006/2007, a major SSW occurred on February 23. However, this event had little impact on the evolution of $z_{eq}{}^{d}$. More pronounced variations in $z_{eq}{}^{d}$ can be seen in mid-January (a drop to ~77 km), which can be associated, similarly to 2005, with a local increase in the zonal wind to ~50 m/s.~~

~~In 2007/2008, there were four SSW events: three consecutive minor SSWs and one major event occurring on 25 January, 2 February, 16 February, and 23 February, respectively (Wang and Alexander, 2009). During this period, $z_{eq}{}^{d}$ demonstrated~~ In 2008 (Figure 6), $z_{eq}{}^{d}$ exhibited pronounced quasi-periodic oscillations with a period of ~~~~approximately 7–10 days ~~in the range of 78–84~~at altitudes between 77 and 83 km. ~~At least five~~Five distinct maxima ~~of~~in the NOCE boundary height ~~can be~~are observed on 23 January, 3 February, 14 February, 21 February, and 3 March. ~~Thus, the first four $z_{eq}{}^{d}$ maxima can be attributed to the occurrence of SSWs, whereas the last one could~~Wang and Alexander (2009) identified four SSW events during this period: three consecutive minor SSWs and one major event, occurring on 25 January, 2 February, 16 February, and 23 February, respectively. The height–time temperature evolution derived from SABER observations (Figure S3) indicates that these SSWs induced quasi-periodic temperature oscillations at 80°N above 70 km, with minima coinciding with the SSW events. As shown in Section 3, the NOCE boundary is strongly sensitive to temperature. Notably, these temperature oscillations are consistent with JAWARA reanalysis data (Figure S9 in Yamazaki et al., 2025). Thus, the first four $z_{eq}{}^{d}$ oscillations can be attributed to the SSWs, whereas the fifth may be a manifestation of the seasonal restructuring of stratospheric dynamics~~ with~~, characterized by oscillations of the mean zonal wind ~~around~~about zero (Wang and Alexander, 2009).

~~Evidently, the major SSW in early 2009 was one of the most powerful phenomena with an elevated stratopause ever observed. The central date was determined to be January 24, but 3 days prior, $z_{eq}{}^{d}$ rapidly~~

~~(over 5–6 days) rose from ~79 km to ~87 km. The subsequent decline of $z_{eq}{}^{d}$ below 73.5 km is attributed to the elevated stratopause rising from ~20 km to ~82 km (Yamazaki et al., 2025), which jumped to this altitude around January 31. Note that~~ In 2015, due to the SABER satellite measurement geometry, the evolution of $z_{eq}{}^{d}$ began with a sharp drop from 84 km to 78 km (Figure 7). Manney et al. (2015) noted that this winter was characterized by ~~the longest-lasting elevated stratopause, so the minimum values of $z_{eq}{}^{d}$ persisted for ~3 weeks, delaying the recovery.~~

~~In 2009/2010, the central date of the major SSW was February 9. That winter, the evolution of $z_{eq}{}^{d}$ demonstrated two peaks (~83.5 and 84.5 km), one of which approximately corresponded to the major SSW. The elevated stratopause was weakly developed (from ~50 km to ~72 km, Yamazaki et al., 2025) and short-lived, so the NOCE boundary height did not fall below 77.5–78 km.~~

~~The winter of 2010/2011 was strong, and only a minor SSW was detected on February 1. Before this event, $z_{eq}{}^{d}$ dropped from ~82 to ~77 km, possibly due to zonal wind strengthening. As a result, the subsequent minor SSW led to the recovery of the NOCE boundary height to ~82 km.~~

~~The winter of 2011/2012 is notable because there was only a minor SSW (January 11), followed by an elevated stratopause. There was a small jump in $z_{eq}{}^{d}$ from 80 km to 82 km due to this SSW. The subsequent elevated stratopause, rising from ~40 km to ~80 km (Yamazaki et al., 2025), led to a drop in $z_{eq}{}^{d}$ to ~76 km at the end of January, followed by a quick recovery to ~80 km in mid-February.~~

~~The winter of 2012/2013 was characterized by a powerful major SSW (January 7) followed by an elevated stratopause rising from ~35 km to ~80 km (Yamazaki et al., 2025). As in the cases of 2006 and 2009, intense variations in the NOCE boundary height at 80°N can be seen: a rapid rise of this characteristic from ~80 km to ~84.5 km over 3 days, with a subsequent decline below 73 km due to the elevated stratopause. This event persisted for a considerable time, so the minimum values of $z_{eq}{}^{d}$ lasted for ~2 weeks before recovery.~~

~~The winter of 2013/2014 was quite calm with a few minor SSWs that did not greatly disturb either the zonal wind or $z_{eq}{}^{d}$. Weak variations in $z_{eq}{}^{d}$ can be seen within the range of 78–82.5 km without a clear correlation with $U_{60°N,10hPa}$ or $\Delta T_{90-60°N,10hPa}$.~~

~~The winter of 2014/2015 was characterized by~~ an unusual minor SSW in early January ~~with a remarkable~~, which exerted an impact on atmospheric dynamics ~~close~~comparable to that of a major SSW ~~(Manney, 2015).~~. During this ~~time~~period, the zonal wind at 10 hPa reversed above 70°N, ~~which~~a reversal that lasted for only a few days (~~see the~~ purple line in ~~the corresponding panel of~~ Figure 7). ~~Nevertheless~~Consistent with this, a drop in the stratopause was observed, accompanied by ~~warming of~~brief cooling at 80°N above 75 km, as indicated by SABER and JAWARA data; see Figure S4 in the ~~mesopause.~~Supplement and Figure S13 in Yamazaki et al. (2025). Thus, the initial $z_{eq}{}^{d}$ maximum ~~(~~(84~~.6~~ km) at 80°N~~)~~ during this period ~~was caused by the~~can be attributed to this SSW. ~~Note that~~Notably, this

maximum extended from the pole down to 55–60°N (~~see~~ Figure 5). The subsequent strengthening and reconfiguration of the polar vortex ~~and its transformation~~ later in January led to mesopause warming and a ~~drop~~further decrease in $z_{eq}{}^{d}$ to below ~~77~~78 km.

~~The winter of 2015/2016 was strong and cold (Matthias et al., 2016) with one minor SSW occurring on 8–9 February. Nevertheless, before this SSW, there were pronounced oscillations~~Over a two-week period in ~~$U_{60°N,10hPa}$ leading to variations~~January 2020 (Figure 7), a pronounced pulse-like variation in $z_{eq}{}^{d}$ ~~in the 78–83 km range.~~

~~The winter of 2016/2017 was quite calm with a few minor SSWs that did not greatly disturb either the zonal wind or $z_{eq}{}^{d}$. Weak variations in $z_{eq}{}^{d}$ can be seen within the range of 78.5–82.5 km without a clear correlation with $U_{60°N,10hPa}$ or $\Delta T_{90-60°N,10hPa}$.~~

~~In the 2017/2018 winter, there was a strengthening of the stratospheric polar vortex in late December,~~was observed, during which ~~apparently resulted in $z_{eq}{}^{d}$ variations in the 77–82 km range~~it rose from ~~late December~~78 km to 84 km before returning to ~~early January. A major SSW occurred on 12 February 2018. It was accompanied by mesopause warming around 80 km (Yamazaki~~its original level. According to Lawrence et al. (2020) and Lukianova et al~~., 2025), resulting in a decline in $z_{eq}{}^{d}$ from ~83 km to ~77 km until the end of February.~~

~~In the 2018/2019 winter, a powerful major SSW with a subsequent elevated stratopause occurred on January 1, but there was a remarkable gap between the times of polar temperature warming and zonal wind reversal. This is likely the reason why we did not observe a strong $z_{eq}{}^{d}$ rise, as in the previous cases of 2005/2006, 2008/2009, and 2012/2013. On January 9, the stratopause jumped from ~35 to ~80 km (Yamazaki et al., 2025), warming the mesopause and causing $z_{eq}{}^{d}$ to fall to ~72 km.~~

~~The winter of 2019/2020~~ . (2021), this winter was characterized by a remarkably strong stratospheric polar vortex ~~due to~~, driven by unusually weak tropospheric wave activity and wave reflection in the polar upper stratosphere ~~(Lawrence et al., 2020; Lukianova et al., 2021).~~ During the first ~~decade~~10 days of January 2020, a ~~latitude–altitude~~latitudinal and altitudinal splitting of the polar vortex occurred~~,~~. This was accompanied by periodic accelerations in the zonal wind, causing a drop and warming of the stratopause, a zonal wind ~~disturbances~~reversal at mesospheric altitudes (~~see~~purple line in Figure 7 ~~for 2020~~), and mesopause cooling with the formation of a temperature inversion layer ~~formation.~~ (Lukianova et al., 2021). The mesopause cooling can be seen in Figure S5 in the Supplement and Figure S15 in Yamazaki et al. (2025). This event was not a typical SSW ~~caused~~driven by planetary wave breaking. The subsequent strengthening and reconfiguration of the vortex ~~and its transformation~~ later in January led to mesopause warming and the ~~disappearance~~dissipation of the inversion layer. Thus, the ~~pronounced~~ pulse-like variation in $z_{eq}{}^{d}$ ~~is~~was a manifestation of the ~~polar vortex's own~~intrinsic dynamics of the polar vortex, rather than a classical warming ~~due to~~event driven by the ~~breakdown~~breaking of upward-propagating planetary waves

~~from the troposphere~~.

~~In the 2020/2021 winter, a powerful major SSW occurred on January 4, which corresponded to a noticeable rise in $z_{eq}{}^{d}$ from 79–79.5 km to ~83.5 km and its subsequent return. At the end of January and the beginning of February, two moderate stratopause elevations were observed, from ~54 to ~75 km and from ~55 to ~70 km (Yamazaki et al., 2025), which caused two local oscillations in $z_{eq}{}^{d}$ with a drop to ~76 km.~~

~~The winter of 2021/2022 was quite calm with a stable polar vortex from December to February, leading to weak variations in $z_{eq}{}^{d}$ in the 79–83 km range.~~

~~The winter of 2022/2023 was characterized by a strong polar vortex from December to the first half of January, whose strengthening resulted in a drop in $z_{eq}{}^{d}$ from ~81.5 km to ~76 km on January 1. Subsequent variations in $z_{eq}{}^{d}$ were determined by minor and major SSWs in the second half of January and mid-February, respectively.~~

~~There were a few minor SSWs in the winter of 2023/2024, which did not greatly disturb $z_{eq}{}^{d}$. One can see weak variations $z_{eq}{}^{d}$ within the range of 78–82 km without a clear correlation with $U_{60°N,10hPa}$ or $\Delta T_{90-60°N,10hPa}$.~~

~~There were a few minor SSWs in the winter of 2023/2024, which did not greatly disturb $z_{eq}{}^{d}$. Weak variations in $z_{eq}{}^{d}$ can be seen within the range of 78–82 km without a clear correlation with $U_{60°N,10hPa}$ or $\Delta T_{90-60°N,10hPa}$.~~

~~The winter of 2024/2025 was quite calm with a stable polar vortex from December to February, leading to weak variations in $z_{eq}{}^{d}$ in the 78–82.5 km range.~~

In summary, SSWs without an ES, as well as the internal dynamics of the polar vortex, can lead to pronounced variations in $z_{eq}{}^{d}$ provided such events are accompanied by significant local cooling in the upper mesosphere.

During years with ES events, a clear pattern emerges in the $z_{eq}{}^{d}$ dynamics. We illustrate this using the winter of 2009 (Figure 6), which featured the most intense SSW on record. In the second half of January, a pronounced pulse-like variation in $z_{eq}{}^{d}$ was observed, during which it rapidly rose from 78 km to 86 km over 5–6 days. This pulse coincided closely with the onset of the major SSW (central date: 24 January), which led to extreme cooling (up to 160 K) in the upper mesosphere and mesopause region at 80°N (Figure S3; Figure S10 in Yamazaki et al., 2025). From February to March, we observe: (1) an almost monotonic decrease in $z_{eq}{}^{d}$ to 72.5 km; (2) only minor variations near this level until early March; and (3) a subsequent slow rise in $z_{eq}{}^{d}$. According to SABER (Figure S3) and JAWARA (Figure S10 in Yamazaki et al., 2025) data, this behavior of $z_{eq}{}^{d}$ in February–March can be attributed to the significant (up to 260 K) prolonged warming of the upper mesosphere at 80°N starting on 31 January during the ES

event, when the stratopause ascended abruptly from ~20–30 km to ~82 km.

In 2006 and 2013 (Figure 6), the evolution of $z_{eq}{}^{d}$ was similar to the 2009 case. SABER (Figures S2–S3) and JAWARA (Figures S8 and S12 in Yamazaki et al., 2025) data indicate that the underlying mechanisms were identical. Brief upper mesospheric cooling caused by the SSW led to a pulse in $z_{eq}{}^{d}$, while the subsequent prolonged warming during the ES event manifested as a significant decrease in $z_{eq}{}^{d}$ to ~72 km.

In 2004 (Figure 6), due to SABER's satellite observation geometry, only the second stage associated with the ES is observable (Figure S2), manifesting as a significant, prolonged decrease in $z_{eq}{}^{d}$ to 72 km.

In 2019 (Figure 7), the $z_{eq}{}^{d}$ pulse was weak due to relatively mild upper mesospheric cooling, likely caused by a substantial time lag between the stratospheric warming and the zonal wind reversal. Subsequently, only a significant, prolonged decrease in $z_{eq}{}^{d}$ below 72 km is observed, driven by the prolonged ES (Figure S5; Figure S15 in Yamazaki et al., 2025).

In 2010, two distinct upper mesospheric cooling events occurred: one prior to the major SSW and the second during it (Figure S3; Figure S10 in Yamazaki et al., 2025). This resulted in a two-peaked structure in the $z_{eq}{}^{d}$ evolution (Figure 6). The elevated stratopause was modest in vertical extent (rising from ~50 km to ~70-75 km; Figure S3) and short-lived; consequently, $z_{eq}{}^{d}$ did not fall below 76–77 km.

The 2012 case (Figure 6) is notable because it featured only a minor SSW (11 January), followed by an elevated stratopause. As in 2019, the $z_{eq}{}^{d}$ pulse was muted due to relatively weak upper mesospheric cooling. The subsequent elevated stratopause (Figure S3; Figure S11 in Yamazaki et al., 2025), which rose from ~35 km to ~80-82 km, led to a drop in $z_{eq}{}^{d}$ to ~74 km at the end of January. This was followed by a rapid recovery of $z_{eq}{}^{d}$ to ~78–80 km in mid-February, coinciding with the rapid descent of the stratopause.

In 2021, the elevated stratopause was modest in vertical extent (rising from ~50 km to ~75 km; Figure S5; Figure S16 in Yamazaki et al., 2025) and short-lived; consequently, $z_{eq}{}^{d}$ did not fall below 75 km (Figure 7).

In summary, SSWs accompanied by ES events produce a clear, two-stage pattern in $z_{eq}{}^{d}$ evolution, characterized by fast and slow dynamics driven by the SSW and the subsequent ES, respectively. Throughout these stages, $z_{eq}{}^{d}$ variability is governed by the magnitude and duration of the upper mesospheric cooling and warming, respectively.

Figures 8–9 present contour maps showing the southern latitude–time evolution of $z_{eq}{}^{d}$ in the Southern Hemisphere from June to September between 2002 and 2025~~.~~, derived from SABER data. Compared to the Northern Hemisphere maps in Figures 4–5, significantly weaker $z_{eq}{}^{d}$ variations ~~can be seen~~are observed. The strongest disturbances ~~was above~~occurred poleward of 60°S during the winters of 2002, 2004, 2012, 2014, 2017, and 2023. ~~It is well known that southern SSWs are much rarer than~~

~~northern ones. A major SSW occurred in 2002, which essentially influenced the Antarctic ozone hole that year. The SSW of 2019 was minor but exhibited the largest temperature variations ever recorded in the southern winter polar stratosphere. The winter of 2024 was characterized by two successive minor SSWs in mid-July and early August. Vincent et al. (2025) identified all southern SSWs between 1998 and 2019 using MERRA-2 data. However, most central dates fall outside the time interval where the satellite geometry of SABER allows us to determine $z_{eq}{}^{d}$ above 55°S. Figures 10–11 present the~~ Figure 10 shows typical examples of $z_{eq}{}^{d}$ time evolution ~~of $z_{eq}{}^{d}$ at 80ºS together with $U_{60ºS,10hPa}$ and $\Delta T_{90-60ºS,10hPa}$. In addition, we included the temperature at the 0.1 hPa ($T_{60ºS,0.1hPa}$), calculated using MERRA-2 reanalysis data, as an indicator of lower mesosphere dynamics, and compared its time evolution with that of $z_{eq}{}^{d}$.~~

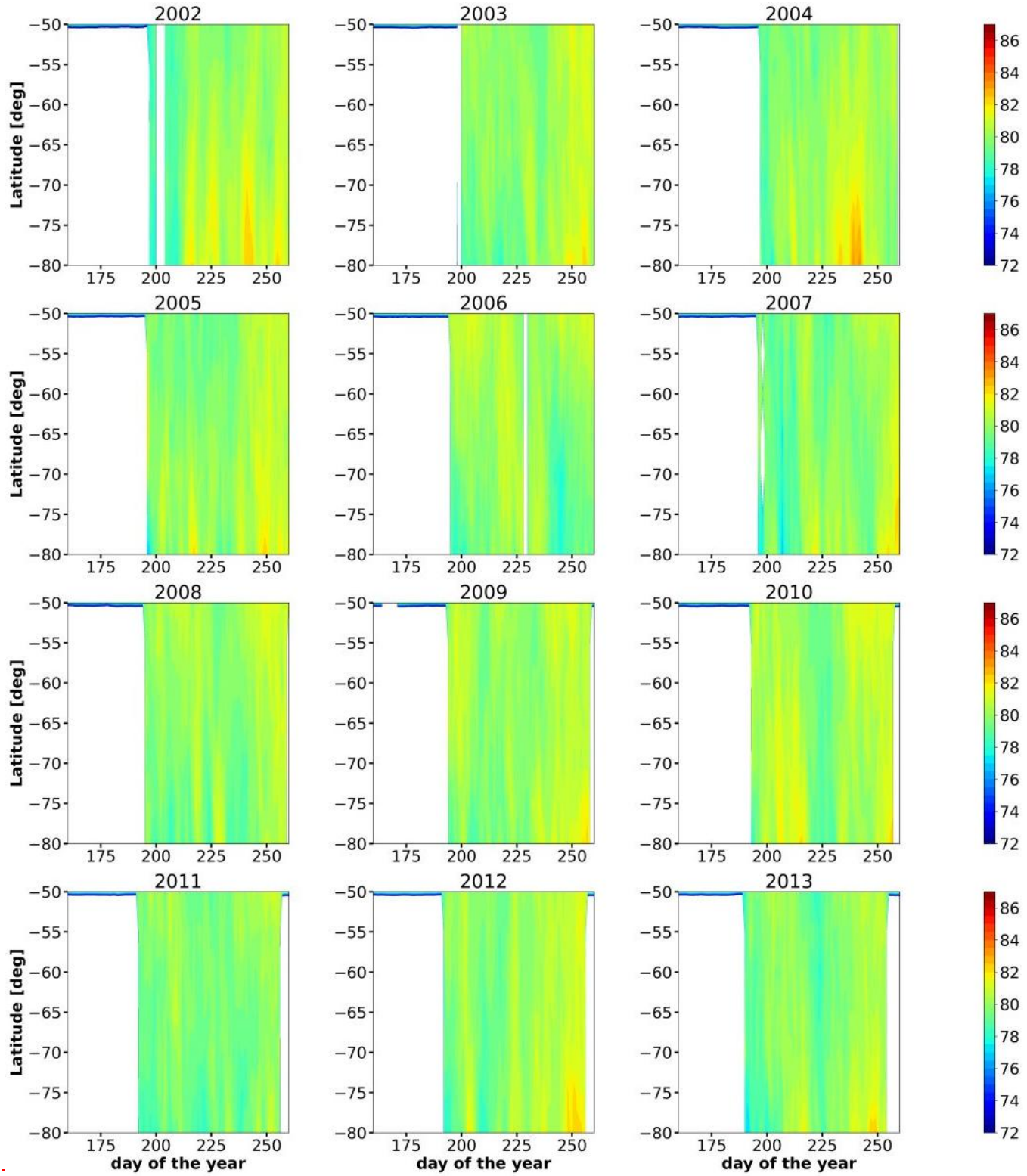
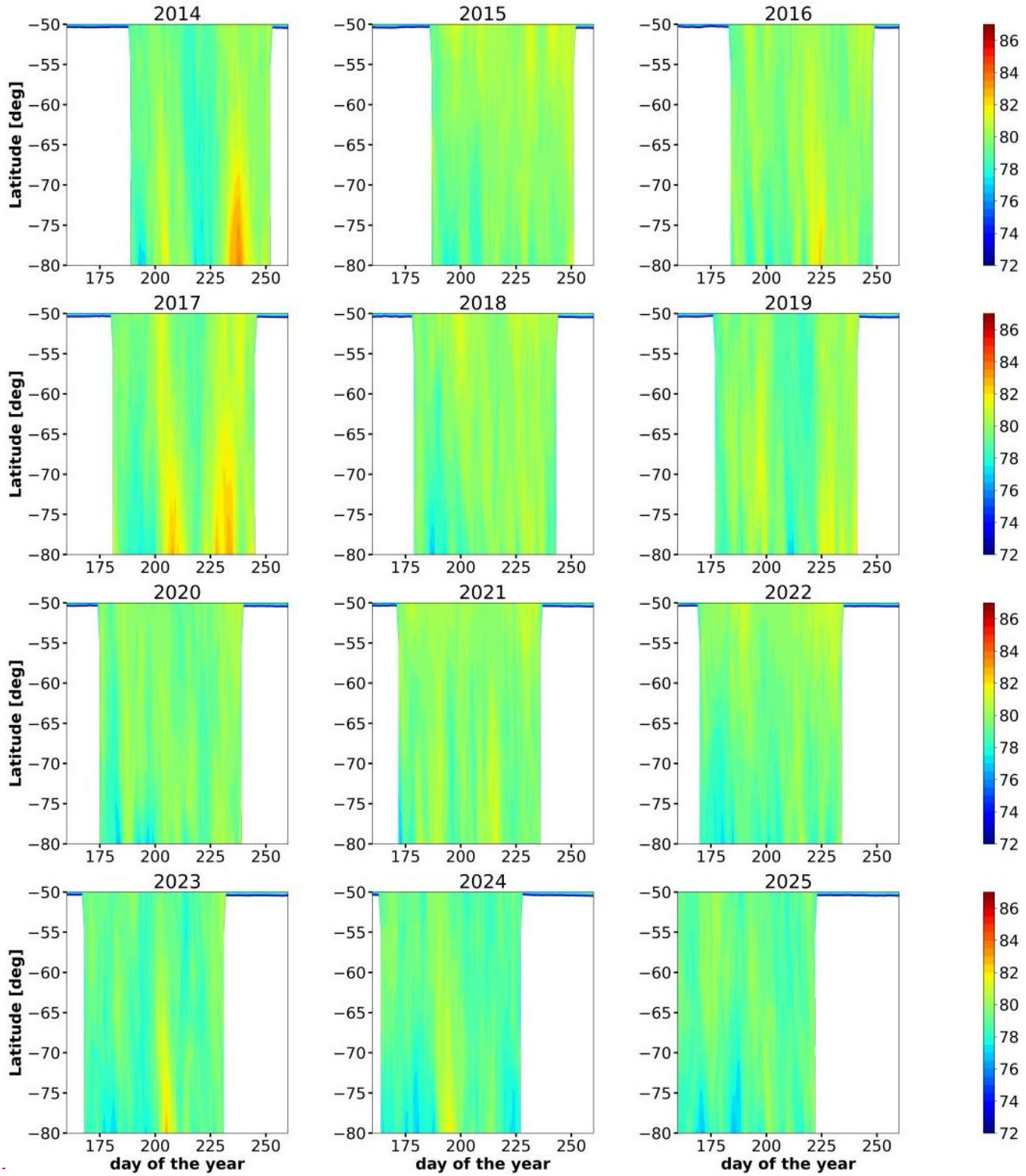
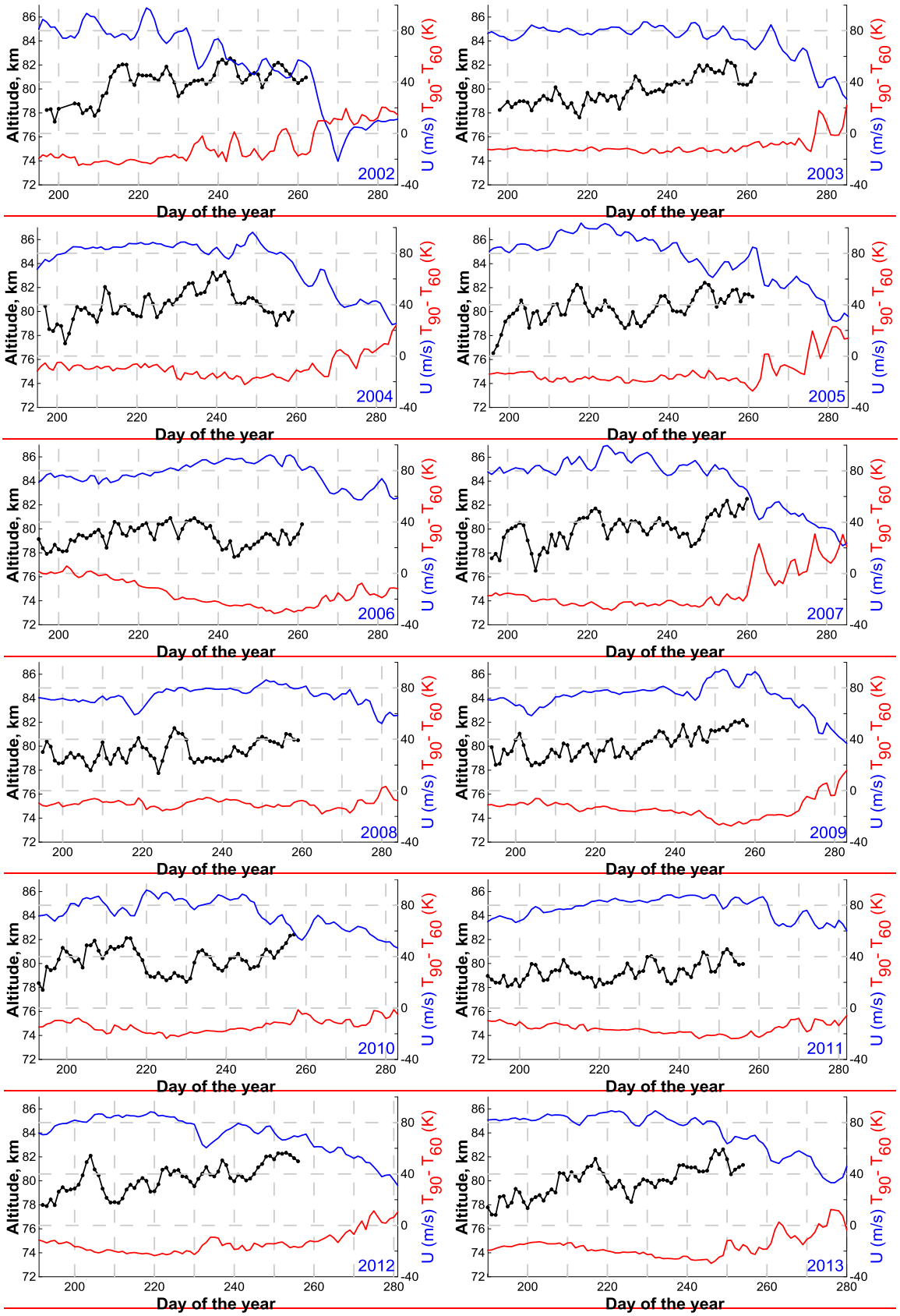


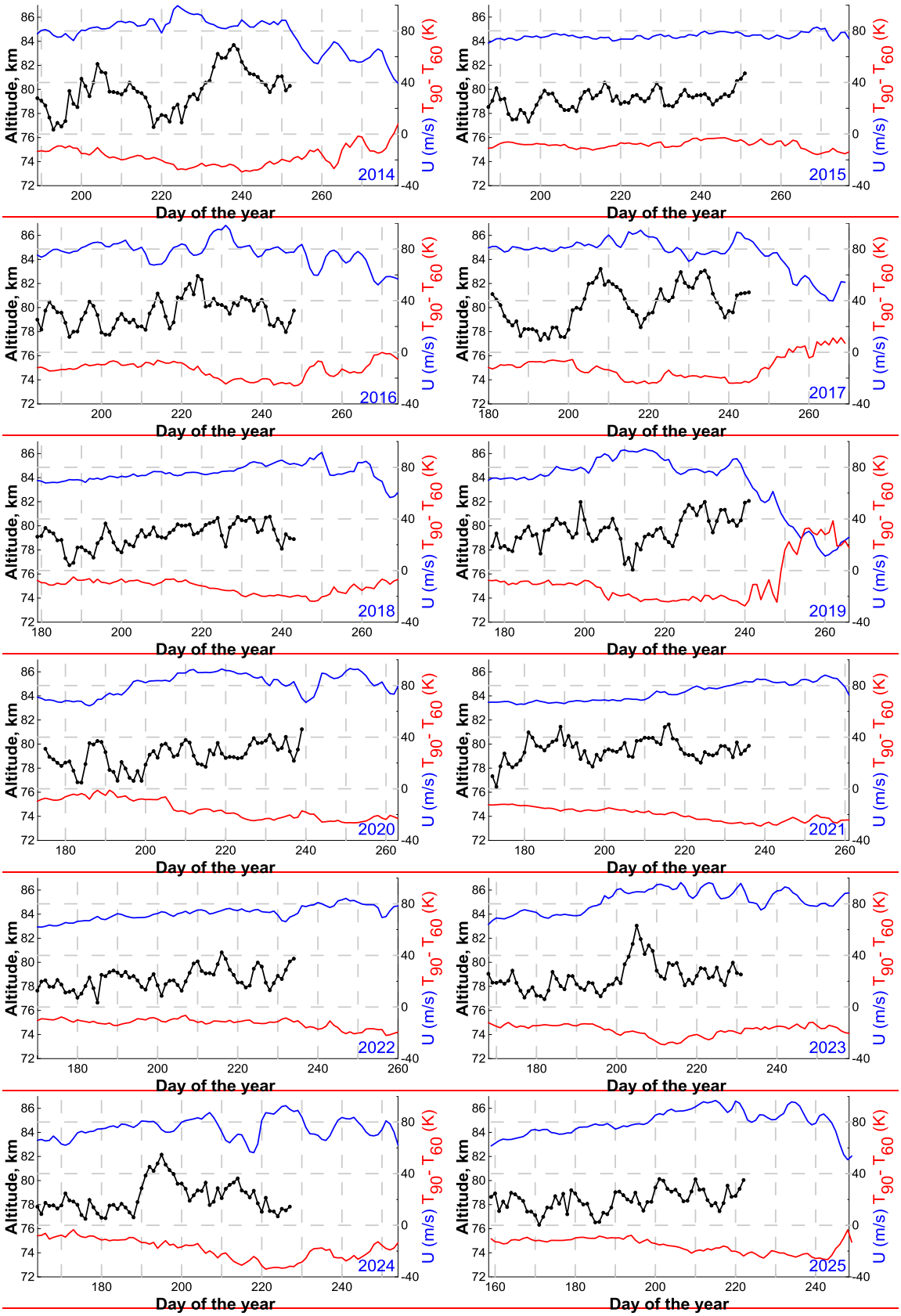
Figure 8. Latitude-time evolution of the daily mean NOCE boundary z_{eq}^{d} at southern polar latitudes in different years.



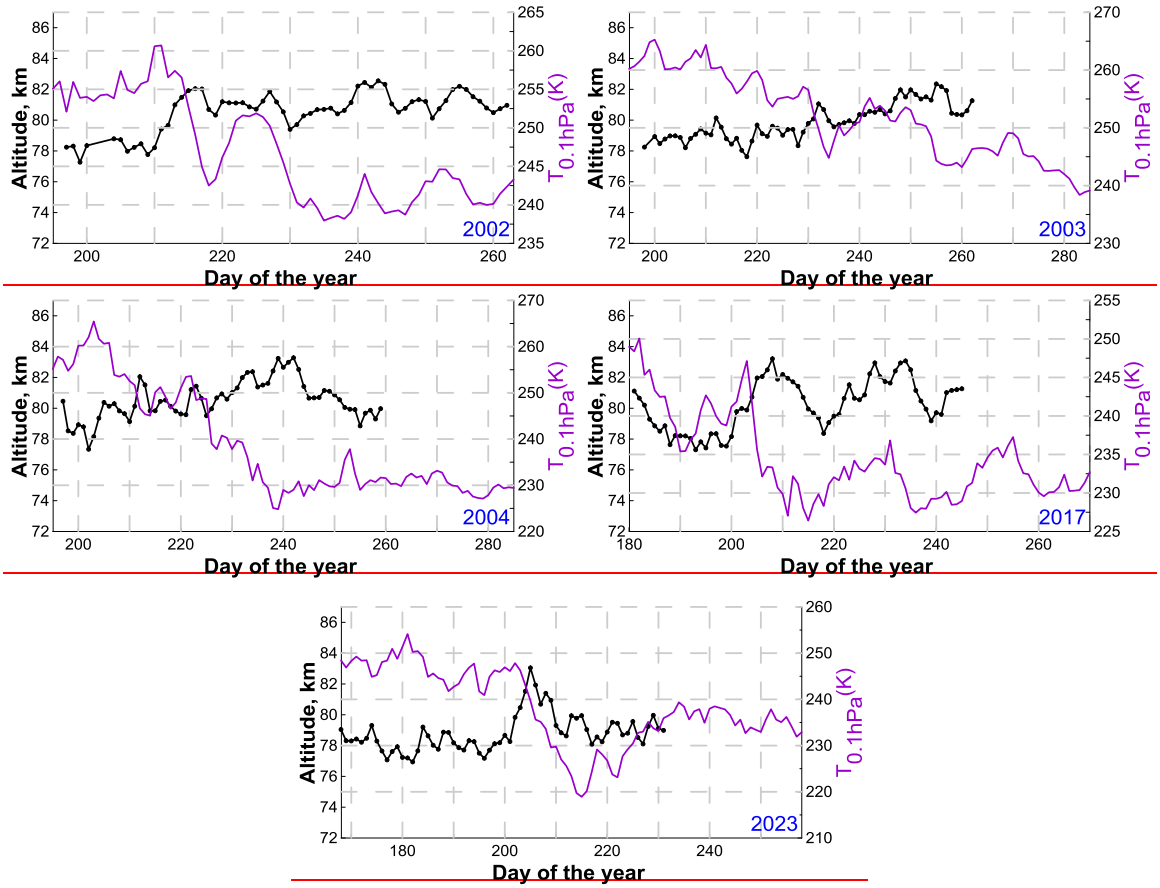
~~Figure 9. Latitude-time evolution of the daily mean NOCE boundary $z_{sq}{}^{d}$ at southern polar latitudes in different years.~~



~~Figure 10. Time evolution of z_{dq}^{d} at 80ºS in different years (black lines with dots). The blue lines show the zonal mean wind at 60ºS and 10hPa, the red lines show the temperature difference between the pole and 60ºS at 10hPa.~~



~~Figure 11. Time evolution of $z_{zq}{}^{d}$ at 80ºS in different years (black lines with dots). The blue lines show the zonal mean wind at 60ºS and 10hPa, the red lines show the temperature difference between the pole and 60ºS at 10hPa.~~



~~Figure 12. Time evolution of $z_{eq}{}^{d}$ at 80ºS (black lines with dots) versus the temperature at 60ºS and 0.1hPa in the~~ at 80°S for selected years~~.~~, derived from SABER data.

~~The presented~~Note that the central dates of most Southern Hemisphere SSWs fall outside the time ~~evolution~~intervals when SABER's orbital geometry permits the determination of $z_{eq}{}^{d}$ ~~at 80~~poleward of 55°S ~~can be classified into one of four types: (1) monotonic growth, as in 2003, 2009, 2011, 2015, or 2022; (2) a step-like change, as in~~. In particular, the SSWs of 2002~~, or a slope break, as in 2004; (3) an impulse-like disturbance, as in 2012, 2023, or 2024; (4) quasi-periodic oscillations with a period of ~20–30 days, as in 2014 or 2017~~ and 2019 both occurred in September. According to Vincent et al. (2025), the central dates of the minor SSWs ~~in~~between 2002~~–~~ and 2019 that were captured by SABER measurements were 23 August 2002 (day 235~~ of the year~~), 2 September 2002 (day 245), 13 September 2002 (day 256), 6 August 2008 (day 218), 2 August 2010 (day 214), 20 August 2012 (day 233), and 7 September 2013 (day 250). Only ~~a minor manifestation~~weak manifestations of these events ~~can be seen~~are visible in the ~~evolution of~~ $z_{eq}{}^{d}$ evolution shown in Figures 8–10~~ 11. According to~~. Furthermore, Zi et al. (2025~~),~~) reported that the central dates of the two minor SSWs in 2024 were 13 July 2024 (day 195~~ of the year~~) and 4 August 2024 (day 217). ~~It can be seen from~~ Figure ~~11~~10 (the panel for 2024) shows that the first event corresponded to a local $z_{eq}{}^{d}$ rise from ~77 km to ~82 km, ~~but~~whereas the second ~~one~~ did not significantly ~~disturb~~perturb $z_{eq}{}^{d}$. ~~A comparison with the~~

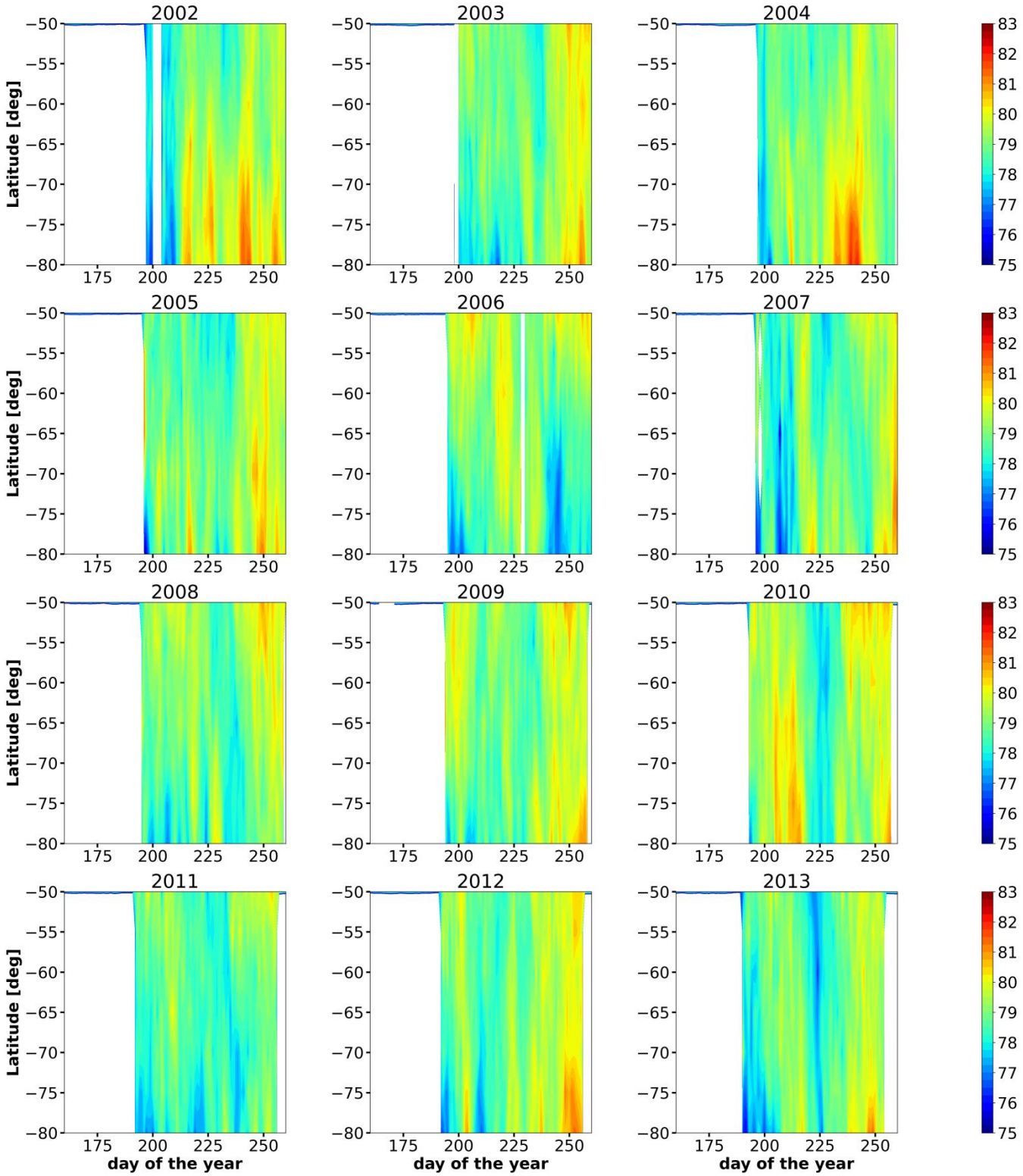


Figure 8. Latitude-time evolution of the daily mean NOCE boundary ${z_{eq}}^{d}$ (geometrical altitude, km) at southern polar latitudes in 2002-2013 obtained from SABER data. White areas indicate missing data due to satellite geometry.

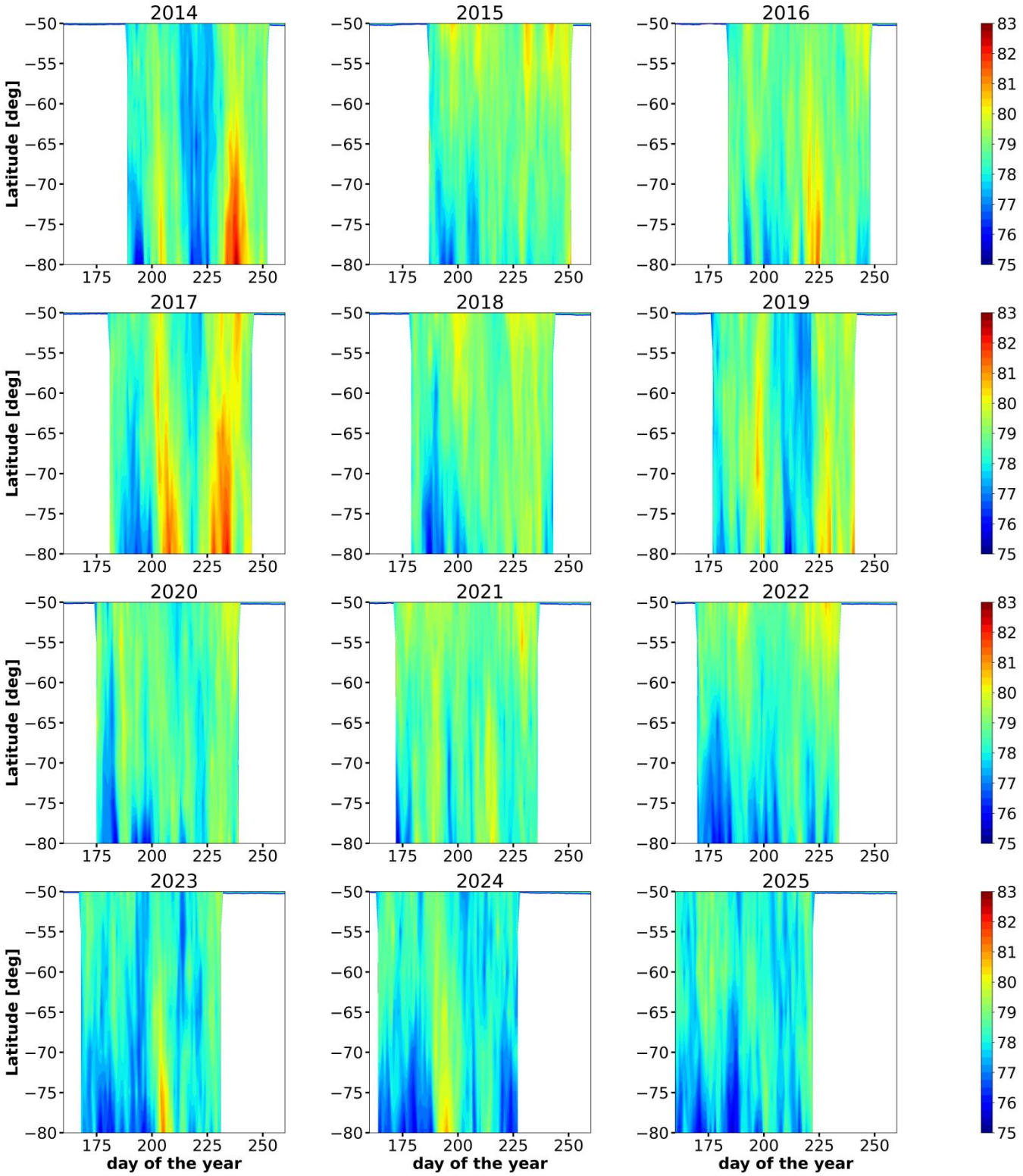


Figure 9. Same as Figure 8, but for the period 2014–2025.

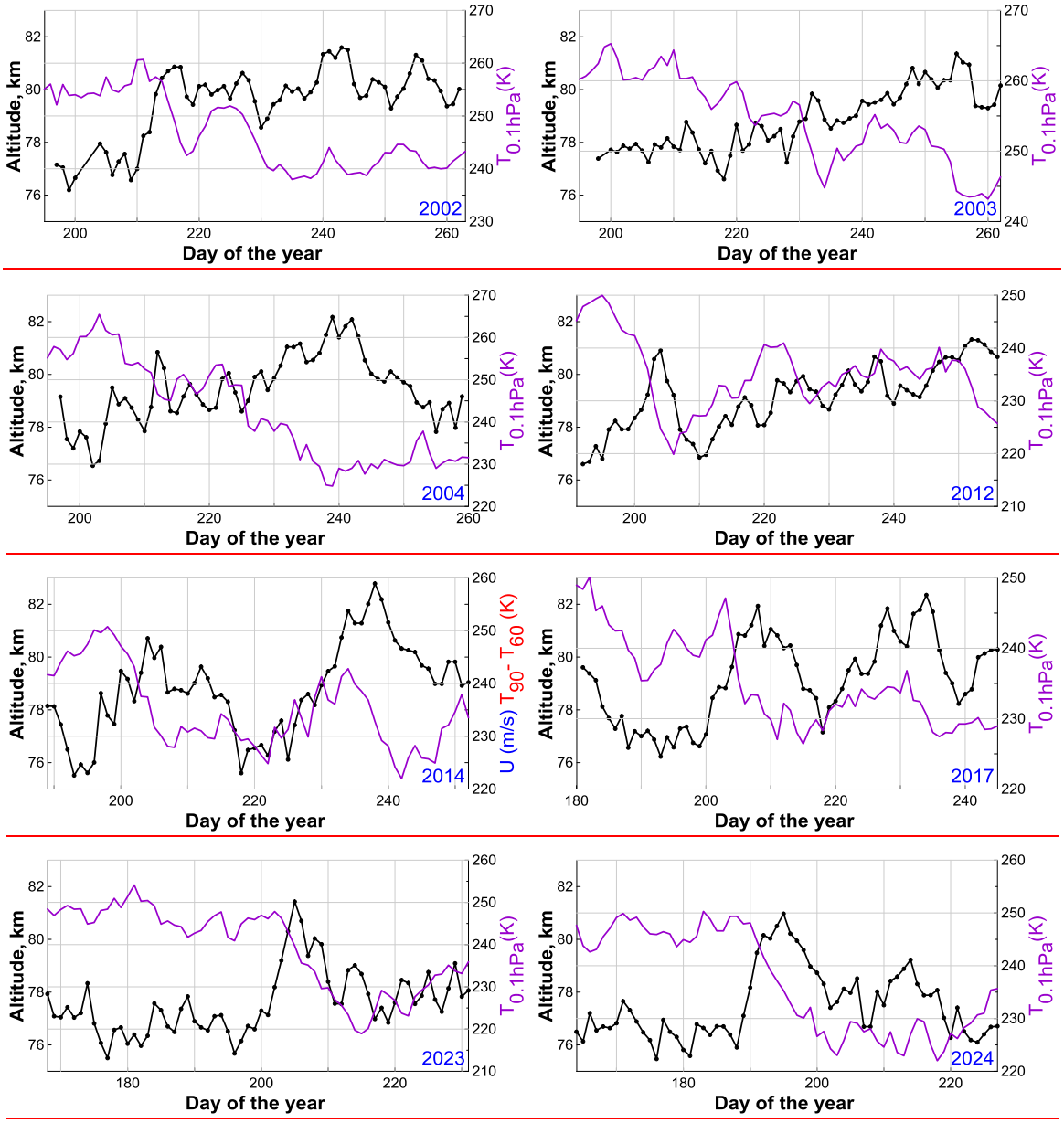


Figure 10. Time evolution of $z_{eq}{}^{d}$ (geometrical altitude) at 80°S (black lines with dots, left y-axis), derived from SABER data for the selected years. Blue lines represent the zonal mean temperature at 60ºS and 0.1 hPa (~~see Figure 12) shows~~right y-axis) from the MERRA-2 reanalysis.

The time evolution of $z_{eq}{}^{d}$ at 80°S can be classified into four distinct types: (1) monotonic growth (e.g., 2003); (2) a step-like change (e.g., 2002) or a change in slope (e.g., 2004); (3) a pulse-like disturbance (e.g., 2012, 2023, 2024); and (4) quasi-periodic oscillations with a period of ~20–30 days (e.g., 2014, 2017). A comparison with MERRA-2 temperature data at 60°S and 0.1 hPa ($T_{60ºS,0.1hPa}$), shown in Figure 10, indicates that many features of the $z_{eq}{}^{d}$ evolution can be explained by ~~the~~intrinsic mesospheric dynamics ~~of the polar vortex in the lower mesosphere~~. In particular, the step-like change in $z_{eq}{}^{d}$ in 2002 and the ~~impulse~~pulse in 2023 were accompanied by similar ~~behavior of~~ variations in $T_{60ºS,0.1hPa}$~~; the~~. The monotonic growth of ~~$z_{eq}{}^{d}$~~ $z_{eq}{}^{d}$ in 2003 corresponded to gradual cooling of the lower mesosphere~~:~~, while the change in slope ~~break~~ in 2004 ~~showed~~exhibited a strong anticorrelation (~~with a~~correlation coefficient of

~~-~~0.8) with $T_{60^oS,0.1hPa}$~~; and the~~. Furthermore, the lower mesospheric temperature ~~of the lower mesosphere~~ in 2017 also ~~exhibited~~displayed quasi-periodic~~ oscillations with a period close to that of the $z_{eq}{}^{d}$~~ oscillations with a period closely matching that of the $z_{eq}{}^{d}$ oscillations.

In summary, $z_{eq}{}^{d}$ variations at southern polar latitudes during winter are significantly weaker than those at northern latitudes. These variations are generally decoupled from SSWs and can instead be attributed to intrinsic mesospheric dynamics.

6 Discussion

~~The~~We now show that the sharp change in the diurnal oscillations of O and H above 80 km (discussed in ~~Figure 1~~Section 4) is caused by the strong altitude dependence of ~~the reaction rates that determine the~~their nighttime chemical lifetimes~~ of these components~~. The main loss processes for O at these altitudes are the reactions O + OH → O_2 + H and O + HO_2 → O_2 + OH, whereas the main loss processes for H are the reactions H+HO_2 → O_2+H_2 и H+HO_2 → O+H_2O (Kulikov et al., 2023b). Kulikov et al. (2023a), based on the equations describing purely chemical O and H nighttime evolution, evaluated the nighttime lifetimes of O and H:

$$\tau_O \equiv \frac{O}{|dO/dt|} = \frac{1}{2\cdot k_4\cdot M\cdot O_2}\cdot\left(\frac{O}{H}\right)_{t=t_0} - \left(1-\frac{k_5+k_6}{k_3}\right)\cdot(t-t_0), \quad (~~9~~7)$$

$$\tau_H \equiv \frac{H}{|dH/dt|} = \frac{~~1~~}{~~2\cdot k_4\cdot M\cdot O_2~~}\frac{1}{2\cdot k_4\cdot M\cdot O_2}\cdot\frac{k_3}{k_5+k_6}\cdot\left(\frac{O}{H}\right)_{t=t_0} - \left(\frac{k_3}{k_5+k_6}-1\right)\cdot(t-t_0), \quad (~~10~~8)$$

where t is the local time, t_0 is the onset of night, $\left(\frac{O}{H}\right)_{t=t_0}$ is the O/H ratio at the onset of night. Note that $k_3 \gg k_5 + k_6$ (see Table 1). Above the NOCE boundary: $O_3 \approx O_3{}^{eq} = \frac{k_1\cdot O\cdot O_2\cdot M}{k_2\cdot H}$, then $\left(\frac{O}{H}\right)_{t=t_0} = \frac{(O_3)_{t=t_0}}{M^2}$. Moreover, in the transition zone, relative concentration of ozone (O_3/M) begins to increase, forming a secondary maximum at 90-95 km. This means that the first terms in equations (~~9-10~~7-8) increase with altitude faster than ~~$\frac{1}{M^3}$~~M^{-3}, leading to approximately the same altitude dependence for τ_O and τ_H. Thus, the lower ~~mode~~regim of O and H evolution, characterized by ~~deep~~strong diurnal oscillations, corresponds to the condition $\tau_{O,H} \ll T_n$, where T_n is duration of the night, whereas the weak diurnal oscillations of O and H at higher altitudes correspond to the opposite condition: $\tau_{O,H} \gg$ ~~T_n~~T_n. Consequently, the existence of a narrow transition zone connecting the two ~~modes~~regimes of O and H oscillations is due to a sharp increase in their lifetimes with increasing altitude.

In the ozone equilibrium approximation, criterion (5) can be rewritten as follows:

$$\mathrm{Cr} = 2\cdot\left(k_4\cdot M\cdot O_2\cdot\left(1-\frac{k_5+k_6}{k_3}\right)+k_2\cdot O_3\right)\cdot\frac{1}{k_2\cdot O} \le 0.1. \quad (~~11~~9)$$

It can be seen that the Cr=0.1 contour corresponds to the following expression:

$$k_2\cdot O = 20\cdot\left(k_4\cdot M\cdot O_2\cdot\left(1-\frac{k_5+k_6}{k_3}\right)+k_2\cdot O_3\right), \quad (~~12~~10)$$

which imposes strong constraints on the O concentration at the NOCE boundary. Note that the product $k_4 \cdot M \cdot O_2$ is the dominant term of this relation, which also determines the lifetimes of O and H in (~~9-10~~7-8). As can be seen from Figure 1, at the beginning of the night, the NOCE boundary lies in the region exhibiting ~~deep~~strong diurnal O oscillations. However, since the O concentration at these altitudes drops by 1–2 orders of magnitude or more during the night, the NOCE boundary, according to Equation (~~12~~10), must inevitably rise to those altitudes where a high O concentration persists at the end of the night, i.e., in the region of weak diurnal variations of this component. This is why, during each night, the $\mathrm{Cr} = 0.1$ contour cuts through the transition zone, passing from its lower part to the upper one, and clearly captures its main features (local position and thickness).

In this paper, we determined the NOCE boundary altitude, z_{eq}, using the function $A(T, M, O)$ in (5) with new rate constants corresponding to the OH(v) model of Panka et al. (2021). We carried out an additional analysis to verify the approximation $A(T, M, O) \cong A(T, M, O = 0)$ at the NOCE boundary. For this purpose, we calculated z_{eq} in two ways: assuming $O = 0$ and $O \neq 0$. In the latter case, the atomic oxygen concentration was determined from Eqs. (1) and (3) using the ozone equilibrium condition ($O_3 = {O_3}^{eq}$), following Mlynczak et al. (2013a). Figure 11a shows the difference in z_{eq} values for 2009 as an example. Irrespective of latitude and season, the difference is generally less than 0.01 km, with very rare deviations of up to 0.1–0.2 km, which demonstrates the validity of this approximation. In addition, we compared the z_{eq} values determined using the new and previous rate constants for the function A. We found that the new rate constants led to a systematic downward shift in z_{eq} of approximately 0.5–1.5 km (Figure 11b). Thus, our method for determining the NOCE boundary position is relatively insensitive to the choice of OH* model parameters, demonstrating its robustness.

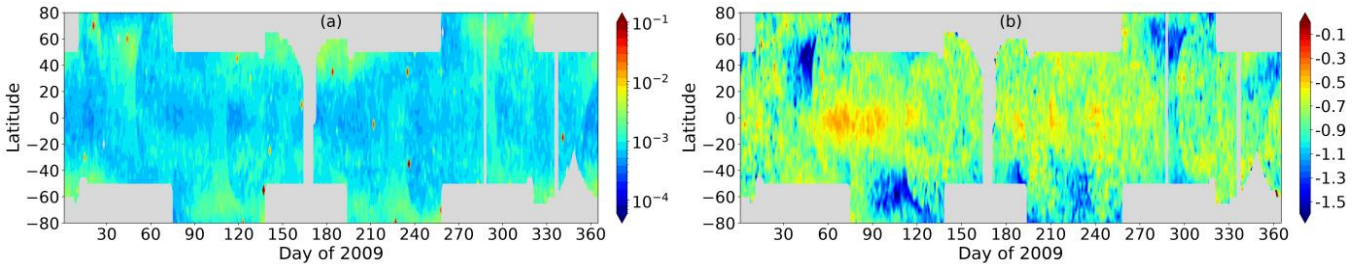
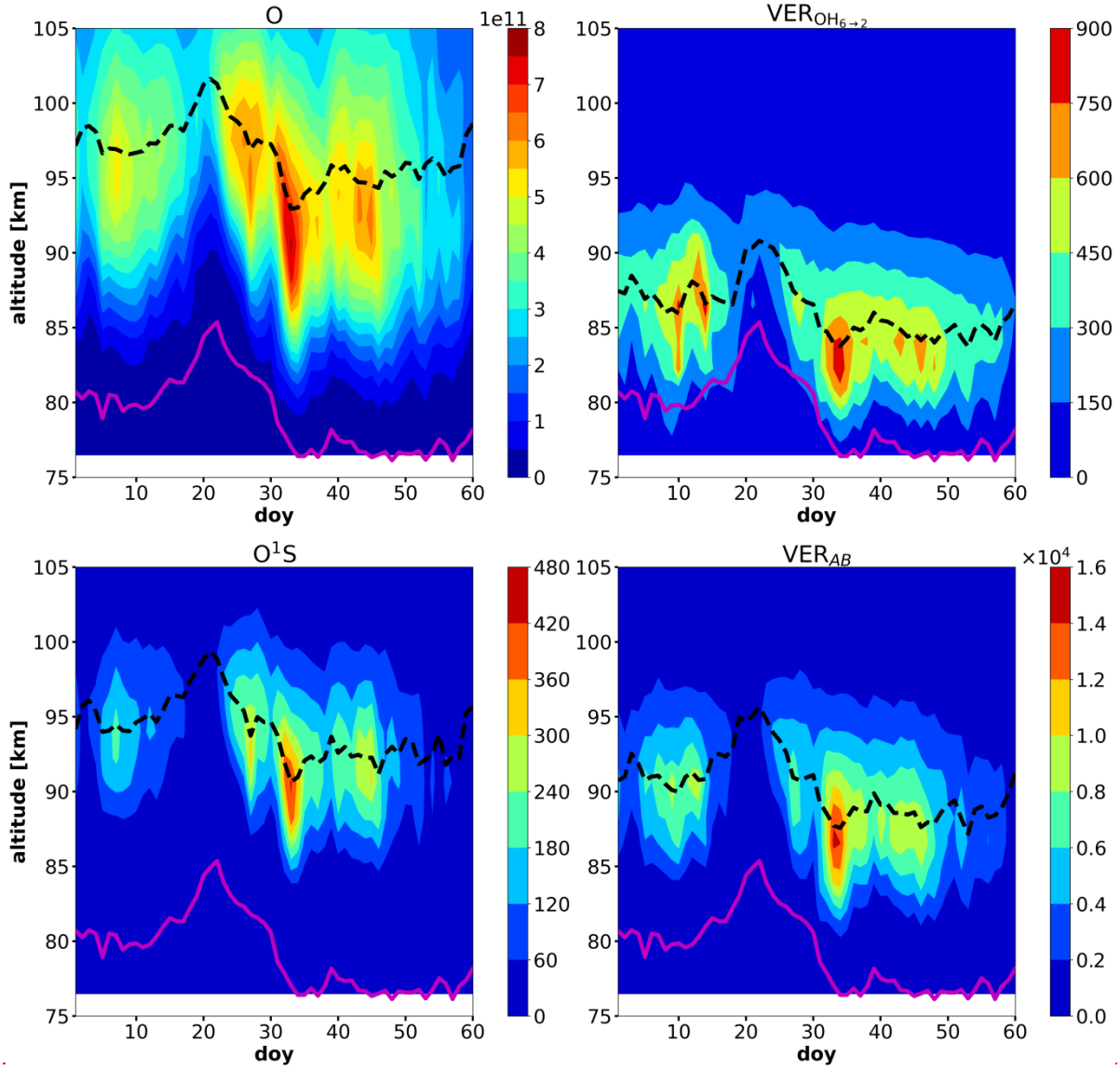


Figure 11. (a) The difference (in km) between ${z_{eq}}^d$ values at 80ºN derived from 2009 SABER data, assuming $O = 0$ and $O \neq 0$. (b) The difference (in km) between ${z_{eq}}^d$ values derived from 2009 SABER data using the new and previous rate constants for function A.

The analysis presented in Section 5 shows that the most pronounced variability of the NOCE boundary at ~~north polar~~high northern latitudes occurs during and after strong SSWs with subsequent elevated stratopause events. Just prior to or directly during such ~~warming~~warmings, the daily mean boundary near the North Pole can ~~jump~~rise abruptly to ~~87~~86 km, and local values may ~~be~~reach even higher

altitudes, up to 90-~~92~~91 km. This ~~means~~implies that during these periods, retrieval methods for ~~retrieving poorly~~sparsely measured mesopause characteristics (in particular, ~~O), based~~atomic oxygen, O) that rely on the ozone equilibrium condition~~,~~ may yield significant ~~uncontrolled~~unquantified errors at altitudes below ~~these altitudes~~ this level due to the breakdown of ~~this~~the equilibrium. ~~At the same time~~Conversely, immediately after such SSWs~~,~~ (during the ES stage), the NOCE boundary rapidly ~~drops down up~~descends to 72~~–~~–74 km and can remain ~~there~~ at these altitudes for ~~a long time.~~

an extended period. Thus, during an ~~elevated stratopause~~ES event, the altitude range over which the ozone equilibrium condition is well satisfied is significantly expanded~~ and can be used for retrieving O and other characteristics well below 80 km. Furthermore, according to Equation (12), such strong variations (first upward, then downward) of the NOCE boundary during such SSWs should reflect specific features of the dynamics of the vertical profile of O and the airglow emissions caused by O_x-HO_x chemistry. Figure 13 presents the evolution of these characteristics in January–February 2009 at ~80°N, simulated using data from the Canadian Middle Atmosphere Model. It can be seen that the NOCE boundary closely follows the variability of the median vertical distributions of O and the volume emission rates of OH(v=1-9), O(^{1}S), and $O_2(b^1\Sigma_g^+)$. Thus, we can assume that the boundary can be used to monitor significant disturbances in both the O_x-HO_x components and the airglows generated by physicochemical processes involving them~~,~~ allowing for the reliable retrieval of O and other characteristics well below 80 km.



~~Figure 13. Time evolution of vertical distributions of O and the volume emission rates of OH(6-2), O(^{1}S) at 557.7 nm, and $O_2(b\,^1\Sigma_g^+)$ at 762 nm (Atmospheric Band) at ~80°N in January–February 2009, simulated using data from the Canadian Middle Atmosphere Model. The black dotted lines show the medians of the presented vertical distributions, magenta line shows the NOCE boundary.~~

The 2009 event (Figure 6) demonstrates the most pronounced variations in $z_{eq}{}^{d}$, particularly during the major SSW that triggered the $z_{eq}{}^{d}$ pulse. A number of studies (e.g., Gao et al., 2012; Medvedeva et al., 2019; Hu et al., 2025) indicate strong perturbations in chemical constituents (specifically, atomic oxygen) and airglow emissions in the mesopause region during both this specific SSW and other major SSWs accompanied by an elevated stratopause. To identify common patterns in the evolution of the NOCE boundary and these characteristics, we examined multiple datasets from various 3D models for 2009 to find one that reproduced the same pulse-like variation in the NOCE boundary during this event. First, we found that the WACCM-X data were unsuitable for this purpose. A likely reason is that the WACCM-X temperature data show a remarkably weaker cooling of the upper mesosphere during this SSW compared

to the SABER data, as can be seen by comparing Figure 1(a) in Hu et al. (2025) with Figure S3 for 2009 in the Supplement. Second, the temperatures from the 2009 annual run of the Canadian Middle Atmosphere Model (CMAM; Scinocca et al., 2008), with 6-hourly output provided by the Canadian Centre for Climate Modelling and Analysis, correspond much better to the SABER data (e.g., Shepherd et al., 2014). We used this run to calculate the daily zonal mean evolution of the NOCE boundary at ~80°N (Figure 12), alongside the daily zonal mean vertical profiles of O and the volume emission rates of OH(6-2), O(^{1}S) at 557.7 nm, and $O_2(b^1\Sigma_g^+)$ at 762 nm (Atmospheric Band). To achieve this, the distributions of OH(v=1-9), O(^{1}S), and $O_2(b^1\Sigma_g^+)$ were calculated using established airglow models driven by CMAM profiles of pressure, temperature, and relevant chemical species (O, H, O_2, and O_3). Specifically, the OH(v=1-9) distributions were derived using the model by Panka et al. (2021; see their Table 1 for details), assuming vibrational level equilibrium. The O(^{1}S) distributions were calculated using the McDade et al. (1986) approximation, with rate constants updated by Gao et al. (2012). Finally, the $O_2(b^1\Sigma_g^+)$ distributions were modeled following Grygalashvyly et al. (2021), utilizing the aforementioned OH(v=1-9) profiles alongside the standard CMAM atmospheric profiles. As shown in Figure 12, the NOCE boundary closely follows the variability of the medians of vertical distributions of O and the airglow emissions. Thus, we can propose that the NOCE boundary can serve as an indicator of disturbances in O_x–HO_x chemistry and the associated airglow variations arising during such powerful SSWs in the mesopause region.

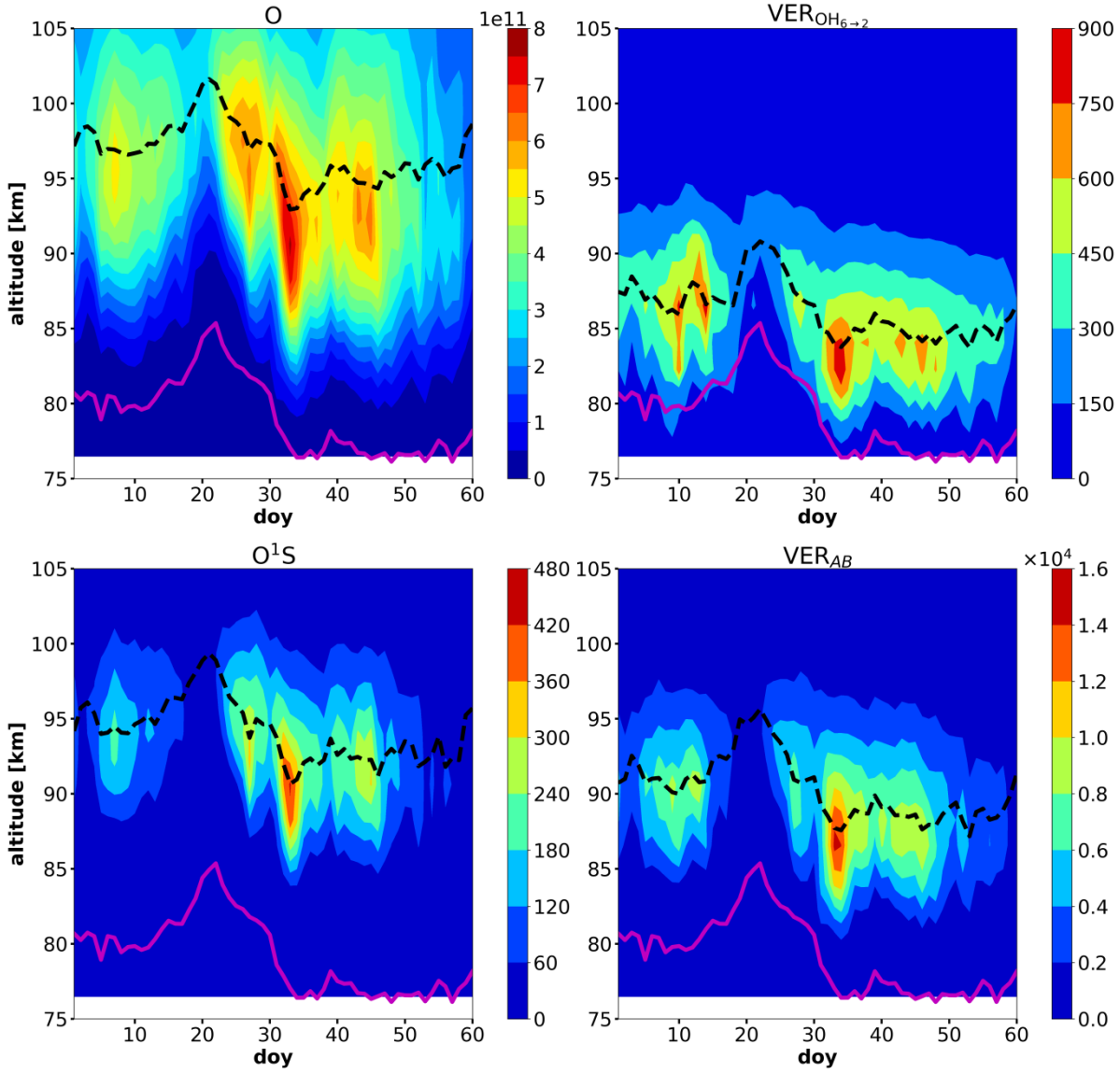


Figure 13. Time evolution of the daily zonal mean profiles (in geometrical altitude) of O (in cm^{-3}) and the volume emission rate (in photon/(cm^3·s)) of OH(6-2), O(^{1}S) at 557.7 nm, and $O_2(b^1\Sigma_g^+)$ at 762 nm (Atmospheric Band) at ~80°N during January–February 2009, simulated using the Canadian Middle Atmosphere Model (CMAM). The black dotted lines indicate the medians of the respective vertical distributions, while the magenta line marks the daily zonal mean NOCE boundary.

7 Conclusions

~~As at mid- and low~~At polar latitudes, the NOCE criterion clearly indicates the local position and thickness of the transition zone separating ~~deep~~pronounced and weak photochemical oscillations of O and H caused by the diurnal variations in solar radiation. This is due to the strong dependence of the NOCE boundary position on the altitude of the layer ~~characterized by~~with a relatively high O concentration. During the polar night, the transition zone effectively "degenerates" into a sharp step in the vertical profiles of these components, and the NOCE criterion identifies the altitude of this step.

~~The~~Based on SABER observations (Figures 4-7), the most pronounced variability of the NOCE

boundary at northern polar latitudes is observed during and after strong SSWs ~~with subsequent~~followed by stratopause elevation events. Just prior to or directly during such warmings, the daily mean altitude of the boundary near the North Pole can jump to 87 km, while local values can be even higher, up to 90–92 km. Immediately after such SSWs, the NOCE boundary rapidly descends to 72–74 km and can remain there for ~~a long time.~~an extended period. Thus, the altitude range where the ozone equilibrium condition is valid ~~to~~for determining O and other mesopause characteristics changes significantly during such events.

Model studies of ~~2009~~the winter of 2009 show that the NOCE boundary ~~well repeat~~closely tracks the variability of the medians of the vertical distributions O and volume emission rates of OH(v=1-9), O(^{1}S), and $O_2(b^1\Sigma_g^+)$.

At southern polar latitudes, variations in the NOCE boundary values during winter are significantly weaker than at northern latitudes. These variations are generally unrelated to minor SSWs during these years, but can instead be explained by the dynamics of the polar vortex in the lower mesosphere.

Data availability. The SABER data are obtained from the website (https://saber.gats-inc.com), last access: 1 July 2026, Mlynczak et al. (2018). CMAM data are obtained from https://climate-modelling.canada.ca/climatemodeldata/cmam/, last access: 1 July 2026, Scinocca et al. (2008). The MERRA-2 data are available publicly from the MERRA-2 website: https://gmao.gsfc.nasa.gov/reanalysis/MERRA-2/, last access: 1 July 2026, Gelaro et al., 2017).

Code availability. As a component of the community earth system model, WACCM-X source code are publicly available at http://www.cesm.ucar.edu), last access: 1 July 2026, Liu et al. (2018).

Author contributions. MK and MB performed data processing and analysis and wrote the manuscript. AC, SD, and AM contributed to reviewing the article.

Competing interests. The authors declare that they have no conflict of interest.

Acknowledgements. The authors are grateful to the SABER team for data availability.

Financial support. The study was supported by the Russian Science Foundation (grant no. 25-27-00242, https://rscf.ru/project/25-27-00242/).

References

Belikovich, M. V., Kulikov, M. Yu, Grygalashvyly, M., Sonnemann, G. R., Ermakova, T. S., Nechaev, A. A., and Feigin, A. M.: Ozone chemical equilibrium in the extended mesopause under the nighttime

conditions, Adv. Space Res., 61, 426–432, https://doi.org/10.1016/j.asr.2017.10.010, 2018.

Belikovich MV, Kulikov MYu, Nechaev AA, Feigin AM ~~(2019)()~~ Evaluation of the atmospheric minor species measurements: a priori statistical constraints based on photochemical modeling~~.~~, Radiophys Quantum El, 61~~:~~, 1–15~~.~~, https://-doi. org/ 10. 1007/ s11141- 019- 09918-5, 2019.

Burkholder, J. B., Sander, S. P., Abbatt, J., Barker, J. R., Cappa, C., Crounse, J. D., Dibble, T. S., Huie, R. E., Kolb, C. E., Kurylo, M. J., Orkin, V. L., Percival, C. J., Wilmouth, D. M., and Wine, P. H.: Chemical Kinetics and Photochemical Data for Use in Atmospheric Studies, Evaluation No. 19, JPL Publication 19-5, Jet Propulsion Laboratory, Pasadena, http://jpldataeval.jpl.nasa.gov, 2020.

~~Evans, W. F. J., McDade, I. C., Yuen, J., and Llewellyn, E. J.: A rocket measurement of the O_2 infrared atmospheric (0-0) band emission in the dayglow and a determination of the mesospheric ozone and atomic oxygen densities, Can. J. Phys., 66, 941–946, https://doi.org/10.1139/p88-151. 1988.~~

Butler, A. H., Seidel, D. J., Hardiman, S. C., Butchart, N., Birner, T., and Match, A.: Defining sudden stratospheric warmings, Bull. Am. Meteorol. Soc., 96, https://doi.org/10.1175/BAMS-D-13-00173.1, 2015.

Hu, J., Gu, S.-Y., Qin, Y., Liu, Y., and Wei, Y.: Influence of sudden stratospheric warming with elevated stratopause on the hydroxyl in the polar middle atmosphere, Atmos. Chem. Phys., 25, 18431–18447, https://doi.org/10.5194/acp-25-18431-2025, 2025.

Feigin, A. M., Konovalov, I. B., and Molkov, Y. I.: Towards understanding nonlinear nature of atmospheric photochemistry: Essential dynamic model of the mesospheric photochemical system., J. Geophys. Res.: Atmos., 103, 25,447–25,460, https://doi.org/10.1029/98JD01569, 1998.

Gao, H., Xu, J., Ward, W., and Smith A. K.: Temporal evolution of nightglow emission responses to SSW events observed by TIMED/SABER, J. Geophys. Res., 116, D19110, https://doi.org/10.1029/2011JD015936, 2011.

Gao, H., Nee, J.-B., Xu, J.: The emission of oxygen green line and density of O atom determined by using ISUAL and SABER measurements, Ann. Geophys., 30, 695–701, https://doi.org/10.5194/angeo-30-695-2012, 2012.

~~Gelaro, R., McCarty, W., Suárez, M. J., Todling, R., Molod, A., Takacs, L., Randles, C. A., Darmenov, A., Bosilovich, M. G., Reichle, R., Wargan, K., Coy, L., Cullather, R., Draper, C., Akella, S., Buchard, V., Conaty, A., da Silva, A. M., Gu, W., Kim, G.-K., Koster, R., Lucchesi, R., Merkova, D., Nielsen, J. E., Partyka, G., Pawson, S., Putman, W., Rienecker, M., Schubert, S. D., Sienkiewicz, M., and Zhao, B.: The modern-era retrospective analysis for research and applications, version 2 (MERRA-2), J. Climate, 30, 5419–5454, https://doi.org/10.1175/JCLI-D-16-0758.1, 2017.~~

Good, R. E.: Determination of atomic oxygen density from rocket borne measurements of hydroxyl airglow, Planet. Space Sci., 24, 389–395, https://doi.org/10.1016/0032-0633(76)90052-0, 1976.

Grygalashvyly, M., Sonnemann, G. R., Lübken, F.-J., Hartogh, P., and Berger, U.: Hydroxyl layer: Mean state and trends at midlatitudes, J. Geophys. Res. Atmos., 119, 12,391–12,419,

https://doi.org/10.1002/2014JD022094, 2014.

Grygalashvyly, M.: Several notes on the OH* layer, Ann. Geophys., 33, 923-930, https://doi.org/10.5194/angeo-33-923-2015, 2015.

Grygalashvyly, M., Strelnikov, B., Eberhart, M., Hedin, J., Khaplanov, M., Gumbel, J., Rapp, M., Lübken, F.-J., Löhle, S., and Fasoulas, S.: Nighttime O(^{1}D) and corresponding Atmospheric Band emission (762 nm) derived from rocket-borne experiment, J. Atmos. Sol.-Terr. Phys., 213, 105522, https://doi.org/10.1016/j.jastp.2020.105522, 2021.

Grygalashvyly, M., Strelnikov, B., Strelnikova, I., Rapp, M., Lübken, F.-J., Schütt, C., Stephan, C., Eberhart, M., Löhle, S., and Fasoulas S.:.Chemical heat derived from rocket-borne WADIS-2 experiment, Earth Planets Space, 76, 180, https://doi.org/10.1186/s40623-024-02129-x, 2024.

~~Feigin, A.~~Kalogerakis, K. S., Matsiev, D., Sharma, R. D., and Wintersteiner, P. P.: Resolving the mesospheric nighttime 4.3 μm emission puzzle: Laboratory demonstration of new mechanism for OH(υ) relaxation, Geophys. Res. Lett., 43(17), 8835–8843, https://doi.org/10.1002/2016GL069645, 2016.

~~M., Konovalov, I. B., and Molkov, Y. I.: Towards understanding nonlinear nature of atmospheric photochemistry: Essential dynamic model of the mesospheric photochemical system., J. Geophys. Res.: Atmos., 103, 25,447–25,460, https://doi.org/10.1029/98JD01569, 1998.~~

~~Konovalov, I. B., and Feigin, A. M.: Towards an understanding of the non-linear nature of atmospheric photochemistry: origin of the complicated dynamic behavior of the mesospheric photochemical system, Nonlin. Processes Geophys., 87-104, https://doi.org/10.5194/npg-7-87-2000, 2000.~~

Kowalewski, S., v. Savigny, C., Palm, M., McDade, I. C., and Notholt, J.: On the impact of the temporal variability of the collisional quenching process on the mesospheric OH emission layer: a study based on SD-WACCM4 and SABER, Atmos. Chem. Phys., 14, 10193-10210, https://doi.org/10.5194/acp-14-10193-2014, 2014.

Kulikov, M. Yu., and Feigin, A. M.: Reactive-diffusion waves in the mesospheric photochemical system. Adv. Space Res., 35(11), 1992-1998, https://doi.org/10.1016/j.asr.2005.04.020, 2005.

Kulikov, M. Y., Feigin, A. M., and Sonnemann, G. R.: Retrieval of the vertical distribution of chemical components in the mesosphere from simultaneous measurements of ozone and hydroxyl distributions, Radiophys Quantum El., 49, 683–691, https://doi.org/10.1007/s11141-006-0103-4, 2006.

Kulikov, M. Yu.: Theoretical investigation of the influence of a quasi 2-day wave on nonlinear photochemical oscillations in the mesopause region, J. Geophys. Res., 112, D02305, https://doi.org/10.1029/2005JD006845, 2007.

Kulikov, M. Y., Feigin, A. M., and Sonnemann, G. R.: Retrieval of water vapor profile in the mesosphere from satellite ozone and hydroxyl measurements by the basic dynamic model of mesospheric photochemical system, Atmos. Chem. Phys., 9, 8199–8210, https://doi.org/10.5194/acp-9-8199-2009, 2009.

Kulikov, M. Yu., Vadimova, O. L., Ignatov, S. K., and Feigin, A. M.: The mechanism of non-linear photochemical oscillations in the mesopause region, Nonlin. Processes Geophys., 19, 501–512, https://doi.org/10.5194/npg-19-501-2012, 2012.

Kulikov, M. Y., Belikovich, M. V., Grygalashvyly, M., Sonnemann, G. R., Ermakova, T. S., Nechaev, A. A., and Feigin, A. M.: Daytime ozone loss term in the mesopause region, Ann. Geophys., 35, 677-682 https://doi.org/10.5194/angeo-35-677-2017, 2017.

Kulikov, M. Y., Nechaev, A. A., Belikovich, M. V., Ermakova, T. S., and Feigin, A. M.: Technical note: Evaluation of the simultaneous measurements of mesospheric OH, HO_2, and O_3 under a photochemical equilibrium assumption – a statistical approach, Atm. Chem. Phys., 18, 7453-747, https://doi.org/10.5194/acp-18-7453-2018, 2018a.

Kulikov, M. Y., Belikovich, M. V., Grygalashvyly, M., Sonnemann, G. R., Ermakova, T. S., Nechaev, A. A., and Feigin, A. M.: Nighttime ozone chemical equilibrium in the mesopause region. J. Geophys. Res.,123, 3228–3242, https://doi.org/10.1002/2017JD026717, 2018b.

Kulikov, M. Yu., Nechaev, A. A., Belikovich, M. V., Vorobeva, E. V., Grygalashvyly, M., Sonnemann, G. R., and Feigin, A. M.: Border of nighttime ozone chemical equilibrium in the mesopause region from saber data: implications for derivation of atomic oxygen and atomic hydrogen, Geophys. Res. Lett., 46, 997–1004, https://doi.org/10.1029/2018GL080364, 2019.

Kulikov, M. Y., Belikovich, M. V., and Feigin, A. M.: Analytical investigation of the reaction-diffusion waves in the mesopause photochemistry, J. Geophys. Res., 125, e2020JD033480, https://doi.org/10.1029/2020JD033480, 2020.

Kulikov, M. Y., Belikovich, M. V., Feigin, A. M.: The 2-day photochemical oscillations in the mesopause region: the first experimental evidence? Geophys. Res. Lett., 48, e2021GL092795, https://doi.org/10.1029/2021GL092795, 2021.

Kulikov M. Yu., Belikovich, M. V., Grygalashvyly, M., Sonnemann, G. R., and Feigin, A. M.: Retrieving daytime distributions of O, H, OH, HO_2, and chemical heating rate in the mesopause region from satellite observations of ozone and OH* volume emission: The evaluation of the importance of the reaction $H+O_3 \rightarrow O_2+OH$ in the ozone balance, Adv. Space Res., 69, 3362–3373,https://doi.org/10.1016/j.asr.2022.02.011, 2022a.

Kulikov, M. Y., Belikovich, M. V., Grygalashvyly, M., Sonnemann, G. R., and Feigin, A.M.: The revised method for retrieving daytime distributions of atomic oxygen and odd-hydrogens in the mesopause region from satellite observations, Earth Planets Space, 74, 44, https://doi.org/10.1186/s40623-022-01603-8, 2022b.

Kulikov, M. Yu., Belikovich, M. V., Chubarov, A. G., Dementyeva, S. O., and Feigin, A. M.: Boundary of nighttime ozone chemical equilibrium in the mesopause region: long-term evolution determined using 20-year satellite observations, Atmos. Chem. Phys., 23, 14593–14608, https://doi.org/10.5194/acp-23-14593-

2023, 2023a.

Kulikov, M. Yu., Belikovich, M. V., Chubarov, A. G., Dementeyva, S. O., Feigin, A. M.: Boundary of nighttime ozone chemical equilibrium in the mesopause region: improved criterion of determining the boundary from satellite data, Adv. Space Res., 71 (6), 2770-2780, https://doi.org/10.1016/j.asr.2022.11.005, 2023b.

Lawrence, Z. D., Perlwitz, J., Butler, A. H., Manney, G. L., Newman, P. A., Lee, S. H., Nash, E. R.: The remarkably strong Arctic stratospheric polar vortex of winter 2020: Links to record-breaking Arctic Oscillation and ozone loss, J. Geophys. Res. Atmos., 125, e2020JD033271, https://doi.org/10.1029/2020JD033271, 2020.

Liu, H.-L., Bardeen, C. G., Foster, B. T., Lauritzen, P., Liu, J., Lu, G., Marsh, D. R., Maute, A., McInerney, J. M., Pedatella, N. M., Qian, L., Richmond, A. D., Roble, R. G., Solomon, S. C., Vitt, F. M., Wang, W.: Development and validation of the Whole Atmosphere Community Climate Model with thermosphere and ionosphere extension (WACCM-X 2.0), J. Adv. Mod. Earth Sys., 10, 381–402, https://doi.org/10.1002/2017MS001232, 2018.

Llewellyn, E. J., ~~McDade, I. C. Moorhouse, P., and Lockerbie, M. D.: Possible reference models for atomic oxygen in the terrestrial atmosphere, Adv. Space Res., 13, 135–144, https://doi.org/10.1016/0273-1177(93)90013-2, 1993.~~

~~Llewellyn, E. J.,~~ and McDade, I. C.: A reference model for atomic oxygen in the terrestrial atmosphere, Adv. Space Res., 18, 209–226, https://doi.org/10.1016/0273-1177(96)00059-2, 1996.

Lukianova, R., Kozlovsky, A., Lester, M.: Upper stratosphere-mesosphere-lower thermosphere perturbations during the formation of the Arctic polar night jet in 2019–2020, Geophys. Res. Lett., 48, e2021GL094926, https://doi.org/10.1029/2021GL094926, 2021.

Manney, G. L., Kruger, K., Sabutis, J. L., Sena, S. A., and Pawson, S.: The remarkable 2003–2004 winter and other recent warm winters in the Arctic stratosphere since the late 1990s. J. Geophys. Res., 110, D04107, https://doi.org/10.1029/2004JD005367, 2005.

Manney, G. L., Lawrence, Z. D., Santee, M. L., Read, W. G., Livesey, N. J., Lambert, A., Froidevaux, L., Pumphrey, H. C., and Schwartz, M. J.: A minor sudden stratospheric warming with a major impact: Transport and polar processing in the 2014/2015 Arctic winter, Geophys. Res. Lett., 42, 7808–7816, http://doi.org/10.1002/2015GL065864, 2015.

Marsh, D. R., Smith, A. K., Mlynczak, M. G., and Russell III, J. M.: SABER observations of the OH Meinel airglow variability near the mesopause, J. Geophys. Res., 111, A10S05, https://doi.org/10.1029/2005JA011451, 2006.

Matthias, V., Dörnbrack, A., and Stober, G.: The extraordinarily strong and cold polar vortex in the early northern winter 2015/2016, Geophys. Res. Lett., 43, 12287–12294, doi:10.1002/2016GL071676, 2016.

McDade, I. C., Murtagh, D. P., Greer, R. G. H., Dickinson, P. H. G., Witt, G., Stegman, J., Llewellyn, E.

J., Thomas, L., and ~~Harris, F. R.: Atomic oxygen concentrations~~Jenkins, D. B.: ETON 2: Quenching parameters for the proposed precursors of $O_2(b^1\Sigma_g^+)$ and $O(^1S)$ in the ~~lower auroral thermosphere, Adv~~terrestrial nightglow, Planet. Space ~~Res., 5, 229–232~~Sci., 34, 789–800, https://doi.org/10.~~1029/GL011I003P00247, 1985~~1016/0032-0633(86)90075-9, 1986.

McDade, I. C., and Llewellyn, E. J.: Mesospheric oxygen atom densities inferred from night-time OH Meinel band emission rates, Planet. Space Sci., 36, 897–905, https://doi.org/10.1016/0032-0633(88)90097-9, 1988.

Medvedeva, I. V., Semenov, A. I., Pogoreltsev, A. I., and Tatarnikov, A. V.: Influence of sudden stratospheric warming on the mesosphere/lower thermosphere from the hydroxyl emission observations and numerical simulations, J. Atmos. Solar-Terr. Phys., 187, 22-32, https://doi.org/10.1016/j.jastp.2019.02.005, 2019.

Mlynczak, M. G., Marshall, B. T., Martin-Torres, F. J., Russell III, J. M., Thompson, R. E., Remsberg, E. E., and Gordley, L. L.: Sounding of the Atmosphere using Broadband Emission Radiometry observations of daytime mesospheric $O_2(^1$~~D~~$^1\Delta)$ 1.27 μm emission and derivation of ozone, atomic oxygen, and solar and chemical energy deposition rates, J. Geophys. Res., 112, D15306, https://doi.org/10.1029/2006JD008355, 2007.

Mlynczak, M. G., Hunt, L. A., Mast, J. C., Marshall, B. T., Russell III, J. M., Smith, A. K., Siskind, D. E., Yee, J.-H., Mertens, C. J., Martin-Torres, F. J., Thompson, R. E., Drob, D. P., and Gordley, L. L.: Atomic oxygen in the mesosphere and lower thermosphere derived from SABER: Algorithm theoretical basis and measurement uncertainty, J. Geophys. Res., 118, 5724–5735, https://doi.org/10.1002/jgrd.50401, 2013a.

Mlynczak, M. G., Hunt, L. H., Mertens, C. J., Marshall, B. T., Russell III, J. M., López-Puertas, M., Smith, A. K., Siskind, D. E., Mast, J. C., Thompson, R. E., and Gordley, L. L.: Radiative and energetic constraints on the global annual mean atomic oxygen concentration in the mesopause region, J. Geophys. Res. Atmos., 118, 5796–5802, https://doi.org/10.1002/jgrd.50400, 2013b.

Mlynczak, M. G., Hunt, L. A. Marshall, B. T. Mertens, C. J. Marsh, D. R. Smith, A. K. Russell, J. M. Siskind D. E., and Gordley L. L.: Atomic hydrogen in the mesopause region derived from SABER: Algorithm theoretical basis, measurement uncertainty, and results, J. Geophys. Res., 119, 3516–3526, https://doi.org/10.1002/2013JD021263, 2014.

Mlynczak, M. G., Hunt, L. A., Russell, J. M. III, and Marshall, B. T.: Updated SABER night atomic oxygen and implications for SABER ozone and atomic hydrogen, Geophys. Res. Lett., 45, 5735–5741, https://doi.org/10.1029/2018GL077377, 2018.

Molod, A., Takacs, L., Suarez, M., and Bacmeister, J.: Development of the GEOS-5 atmospheric general circulation model: evolution from MERRA to MERRA2, Geosci. Model Dev., 8, 1339–1356, https://doi.org/10.5194/gmd-8-1339-2015, 2015.

Nikoukar, R., Swenson, G. R., Liu, A. Z., and Kamalabadi, F.: On the variability of mesospheric OH

emission profiles, J. Geophys. Res., 112, D19109, https://doi.org/10.1029/2007JD008601, 2007.

Panka, P. A., Kutepov, A. A., Zhu, Y., Kaufmann, M., Kalogerakis, K. S., Rezac, L., Feofilov, A. G., Marsh, D. R., and Janches, D.: Simultaneous retrievals of nighttime O(^{3}P) and total OH densities from satellite observations of Meinel band emissions, Geophys. Res. Lett., 48, e2020GL091053, https://doi.org/10.1029/2020GL091053, 2021.

Pendleton, W. R., Baker, K. D., Howlett, L. C.: Rocket-based investigations of O(^{3}P), O_2 ($a^1\Delta_g$) and OH* (v=1,2) during the solar eclipse of 26 February 1979, J. Atm. Terr. Phys., 45(7), 479-491, 1983.

~~Siskind, D. E., Marsh, D.~~Roy, R., ~~Mlynczak, M. G., Martin-Torres, F.~~Kuttippurath, J., Lefèvre, F., and ~~Russell III, J. M.: Decreases~~Kumar, P.: The sudden stratospheric warming and chemical ozone loss in ~~atomic hydrogen over~~ the ~~summer pole: Evidence for dehydration from polar mesospheric clouds? Geophys. Res. Lett., 35, L13809~~Antarctic winter 2019: comparison with the winters of 1988 and 2002, Theor. Appl. Climatol., 149, 119–130, https://doi.org/10.~~1029/2008GL033742, 2008.~~1007/s00704-022-04031-6, 2022.

Siskind, D. E., Mlynczak, M. G., Marshall, T., Friedrich, M., Gumbel, J.: Implications of odd oxygen observations by the TIMED/SABER instrument for lower D region ionospheric modeling, J. Atmos. Sol. Terr. Phys., 124, 63–70, https://doi.org/10.1016/j.jastp.2015.01.014, 2015.

Sharma, R. D., Wintersteiner, P. P., & Kalogerakis, K. S.: A new mechanism for OH vibrational relaxation leading to enhanced CO_2 emissions in the nocturnal mesosphere, Geophys. Res. Lett., 42, 4639–4647, https://doi.org/10.1002/2015GL063724, 2015.

Shepherd, M. G., Beagley, S. R., and Fomichev, V. I.: Stratospheric warming influence on the mesosphere/lower thermosphere as seen by the extended CMAM, Ann. Geophys., 32, 589–608, https://doi.org/10.5194/angeo-32-589-2014, 2014.

Smith, A. K., Lopez-Puertas, M., Garcıa-Comas, M. and Tukiainen, S.: SABER observations of mesospheric ozone during NH late winter 2002–2009, Geophys. Res. Lett., 36, L23804, https://doi.org/10.1029/2009GL040942, 2009.

Smith, A. K., Marsh, D. R. Mlynczak, M. G. and Mast, J. C.: Temporal variations of atomic oxygen in the upper mesosphere from SABER, J. Geophys. Res., 115, D18309, https://doi.org/10.1029/2009JD013434, 2010.

Sonnemann, G., and Fichtelmann, B.: Enforced oscillations and resonances due to internal non-linear processes of photochemical system in the atmosphere, Acta. Geod. Geophys. Mont. Hung., 22, 301–311, 1987.

Sonnemann, G., and Fichtelmann, B.: Subharmonics, cascades of period of doubling and chaotic behavior of photochemistry of the mesopause region, J. Geophys. Res., 101, 1193-1203, https://doi.org/10.1029/96JD02740, 1997.

Sonnemann, G., ~~Kremp, C. Ebel, A. and Berger U.: A three-dimensional dynamic model of minor~~

constituents of the mesosphere, Atmos. Environ., 32, 3157 3172, https://doi.org/10.1016/S1352-2310(98)00113-7, 1998.

Sonnemann, G., Feigin, A. M., and Molkov, Ya. I.: On the influence of diffusion upon the nonlinear behaviour of the photochemistry of the mesopause region, J. Geophys. Res., 104, 30591-30603, https://doi.org/10.1029/1999JD900785, 1999.

Sonnemann, G., and Feigin, A. M.: Non-linear behaviour of a reaction-diffusion system of the photochemistry within the mesopause region, Phys. Rev. E, 59, 1719-1726, https://doi.org/10.1103/PhysRevE.59.1719, 1999.

Sonnemann, G. R., and Grygalashvyly, M.: On the two-day oscillations and the day-to-day variability in global 3-D-modeling of the chemical system of the upper mesosphere/mesopause region, Nonlin. Processes Geophys., 12, 691– 705, https://doi.org/10.5194/npg-12-691-2005, 2005.

Sonnemann, G. R., Hartogh, P., Berger, U., and Grygalashvyly, M.: Hydroxyl layer: trend of number density and intra-annual variability, Ann. Geophys., 33, 749–767, https://doi.org/10.5194/angeo-33-749-2015, 2015.

Scinocca, J. F., McFarlane, N. A., Lazare, M., Li, J., and Plummer, D.: Technical Note: The CCCma third generation AGCM and its extension into the middle atmosphere, Atmos. Chem. Phys., 8, 7055–7074, https://doi.org/10.5194/acp-8-7055-2008, 2008.

Swenson, G. R., and Gardner C. S.: Analytical models for the responses of the mesospheric OH* and Na layers to atmospheric gravity waves, J. Geophys. Res., 103(D6), 6271–6294, https://doi.org/10.1029/97JD02985, 1998.

Thomas, R. J.: Atomic hydrogen and atomic oxygen density in the mesosphere region: Global and seasonal variations deduced from Solar Mesosphere Explorer near-infrared emissions, J. Geophys. Res., 95, 16,457–16,476, https://doi. org/-10.-1029/-JD095 iD10p 16457JD095iD10p16457, 1990.

Vincent, R. A., Kovalam, S., Reid, I. M., Murphy, D. J., Klekociuk, A.: Southern Hemisphere stratospheric warmings and coupling to the mesosphere-lower thermosphere J. Geophys. Res. Atmos., 127, e2022JD036558, https://doi.org/10.1029/2022JD036558, 2022.

Wang, L., and Alexander, M. J.: Gravity wave activity during stratospheric sudden warmings in the 2007–2008 Northern Hemisphere winter, J. Geophys. Res., 114, D18108, http://doi.org/10.1029/2009JD011867, 2009.

Xu, J., Smith, A. K., Jiang, G., Gao, H., Wei, Y., Mlynczak, M. G., and Russell III, J. M.: Strong longitudinal variations in the OH nightglow, Geophys. Res. Lett., 37, L21801, https://doi.org/10.1029/2010GL043972, 2010.

Xu, J., Gao, H. Smith, A. K. and Zhu Y.: Using TIMED/SABER nightglow observations to investigate hydroxyl emission mechanisms in the mesopause region, J. Geophys. Res., 117, D02301, https://doi.org/10.1029/2011JD016342, 2012.

Yamazaki, Y., Sato, K., Koshin, D., Yasui, R., Atmospheric semidiurnal solar tide response to sudden stratospheric warmings in the JAGUAR-DAS Whole neutral Atmosphere Reanalysis (JAWARA) during 2004–2023, J. Geophys. Res. Sp. Phys., 130, e2024JA033688, https://doi.org/10.1029/2024JA033688, 2025.

Zi, Y., Long, Z., Sheng, J., Lu, G., Perrie, W., Xiao, Z.: The sudden stratospheric warming events in the Antarctic in 2024, Geophys. Res. Lett., *52*, e2025GL115257, https://doi.org/10.1029/2025GL115257, 2025.